

Copyright © 1986, by the author(s).
All rights reserved.

Permission to make digital or hard copies of all or part of this work for personal or classroom use is granted without fee provided that copies are not made or distributed for profit or commercial advantage and that copies bear this notice and the full citation on the first page. To copy otherwise, to republish, to post on servers or to redistribute to lists, requires prior specific permission.

**3-D ROTATION INSTRUMENT FOR DISPLAYING
STRANGE ATTRACTORS**

by

L. O. Chua and T. Sugawara

Memorandum No. UCB/ERL M86/61

25 July 1986

3-D ROTATION INSTRUMENT FOR DISPLAYING STRANGE ATTRACTORS

by

L. O. Chua and T. Sugawara

x Memorandum No. UCB/ERL M86/61

25 July 1986

x ELECTRONICS RESEARCH LABORATORY

College of Engineering
University of California, Berkeley
94720

TITLE PAGE

3-D ROTATION INSTRUMENT FOR DISPLAYING STRANGE ATTRACTORS

by

L. O. Chua and T. Sugawara

Memorandum No. UCB/ERL M86/61

25 July 1986

ELECTRONICS RESEARCH LABORATORY

College of Engineering
University of California, Berkeley
94720

3-D ROTATION INSTRUMENT FOR DISPLAYING STRANGE ATTRACTORS†

L.O. Chua

Department of Electrical Engineering and Computer Sciences,
University of California, Berkeley, CA 94720.

T. Sugawaratt

Research and Development Center, Toshiba Corporation,
Kawasaki, 210 Japan.

ABSTRACT

An electronic instrument for displaying any perspective of a 3-dimensional surface S generated by 3 time-varying (not necessarily periodic) signals is described. The surface S is a 3-dimensional Lissajous figure which need not be a closed curve as is typical of all *strange attractors*. This analog (not digital) instrument is designed to rotate S along any axis (not just the X, Y, Z -axis) through any prescribed solid angles ($0^\circ - 360^\circ$) in the 3-dimensional coordinate system in *real time*.

The instrument works as a preprocessor for a standard oscilloscope and is built with components capable of displaying time-varying signals with a frequency spectrum from 0 to 20 K Hz.

To illustrate some immediate applications of this instrument, strange attractors associated with both *autonomous* (Chua's circuit) and *non-autonomous* (Series RL-diode circuit) circuits are presented in many different perspectives and cross sections. In particular, numerous *cross sections* of these strange attractors which have never been seen before can be easily displayed in any *desired perspective* in real time. Such cross sections have proved to be most revealing and invaluable in dissecting and uncovering the fine structures of strange attractors.

†Research partially supported by the office of Naval Research Contract N00014-76-C-0572 and the National Science Foundation Grant ECS-8313278.

†† *T. Sugawara* is currently a visiting scholar at Department of Electrical Engineering and Computer Sciences, University of California, Berkeley, CA 94720.

1. Introduction.

This paper describes the design of a small portable *electronic instrument* which when used with a standard oscilloscope, allows us to display a two-dimensional projection from any desired direction of a 3-dimensional surface S evolving in time. The 3-dimensional surface S represents the dynamic loci of 3 electrical signals $x(t), y(t)$, and $z(t)$ in the $X-Y-Z$ space over some observation time interval, and can be interpreted as the 3-dimensional generalization of the well-known Lissajous figures[1].

At any instant of time $t_0, (x(t_0), y(t_0), z(t_0))$ can be thought of as the position of a particle, or a planet, in our 3-dimensional space. As time evolves, this particle, or a planet, traces out a continuous trajectory. If the motion represented by $(x(t), y(t), z(t))$ is periodic, as is the case of a planet, this trajectory will eventually repeat itself. However, if the motion is not periodic, as is the case in many practical applications, this trajectory never repeats itself and over a long period of time, would fill some volume in space whose overall envelope is a 3-dimensional surface S . This surface is usually extremely complicated with cross sections which are "Fractals" [2] and to analyze its geometric structure would require a detailed analysis of different perspectives and cross sections of S on the oscilloscope screen. It is necessary to take perspectives and cross sections because the oscilloscope can display only 2-dimensional figures.

If we connect 2 of the 3 signals to the horizontal and the vertical channels of the oscilloscope, we could obtain at most 3 possible projections onto the $X-Y, Y-Z$, or $Z-X$ plane, respectively. What we need in practice, however, is to be able to view the projection from any direction. This is analogous to applying a parallel beam of light from any desired direction onto the surface S and then observing its shadow on a white screen behind S . Mathematically, this operation is equivalent to rotating each of the 3 coordinate axis through any desired angle from 0 to 360 degrees and then taking its projection.

Another important operation needed in studying the geometric structure of S is to pass a plane surface D at any desired position in space through S and look at the intersection points between S and D . This set of intersection points is called a cross section of S with

respect to D . In the case of strange attractors, such as the double scroll [3], such cross sections are *fractals*.

One possible approach for implementing the above task is to sample the signals with a high-speed A/D converter and then process the data mathematically by a digital computer before outputting the transformed data into a D/A converter for final display on the oscilloscope.

However, one major problem of this approach is that accurate and high-speed data acquisition and processing currently require very expensive hardwares in addition to a dedicated digital computer. Even then, the displayed signal is no longer in real time. Another limitation of the digital approach is that some of the detailed nature of signals may be lost in the course of data acquisition unless the signals are properly scaled and the resolution of analog-to-digital converter is sufficiently high. An even more serious limitation of the digital approach becomes obvious in the case of complex (non-periodic) dynamics where the sequence of data to be taken is extremely large and may easily exceed the available computer memory.

The instrument to be described in this paper is an *analog* design and therefore has none of the above limitations. In particular, both rotation and cross-section operations are implemented in *real time*.

In Section 2, a brief description of the 3-dimensional rotation geometry is given. Section 3 describes the basic design and block diagram of the 3-D rotation instrument. To illustrate the capability of this instrument, as well as an important application in the study of *chaos* [4], strange attractors and cross sections associated with a *non-autonomous* circuit consisting of a series RL-diode circuit driven by a periodic signal are given in section 4. Similarly, the double scroll and its cross sections as measured from the *autonomous* Chua's circuit [5] are displayed. To the best of our knowledge, many of the pictures given in section 4 and 5 have never been seen before and are therefore of independent interest to researchers in chaotic dynamics.

Finally, section 6 presents some possible modifications of the 3-D rotation instrument as well as some concluding remarks. For readers interested in building this instrument, the detailed circuit diagrams are given in the Appendix.

2. 3-Dimensional Rotation Geometry

In this section, a brief description of the pertinent 3-dimensional rotation geometry is given along with the relation between the actual signal processing and the equivalent mathematical operations.

Consider first the rotation of a 3-dimensional vector $S(t) = [x(t), y(t), z(t)]^T$ as a function of time. For convenience, we call the trajectory of $S(t)$ as a surface S because the envelope of $S(t)$ eventually forms a 3-dimensional surface as time evolves. Strictly speaking, S is a *fractal* [2] if $S(t)$ is associated with a strange attractor.

A. Rotation

Rotation of a vector $S(t)$ is simply an orthogonal transform of $S(t)$, namely,

$$S_o(t) = Q S(t) \quad (2.1)$$

where Q is an *orthogonal* 3-dimensional matrix and $S_o(t)$ is the rotated vector $[x_o(t), y_o(t), z_o(t)]^T$.

The orthogonal matrix Q implemented in our design is defined by its decomposition with respect to the X, Y , and Z axis; namely,

$$Q = R_x(\theta_x) R_y(\theta_y) R_x(\theta_x), \quad (2.2)$$

where

$$R_x(\theta_x) = \begin{bmatrix} 1 & 0 & 0 \\ 0 & \cos(\theta_x) & \sin(\theta_x) \\ 0 & -\sin(\theta_x) & \cos(\theta_x) \end{bmatrix},$$

$$R_y(\theta_y) = \begin{bmatrix} \cos(\theta_y) & 0 & \sin(\theta_y) \\ 0 & 1 & 0 \\ -\sin(\theta_y) & 0 & \cos(\theta_y) \end{bmatrix},$$

and

$$R_x(\theta_x) = \begin{bmatrix} \cos(\theta_x) & \sin(\theta_x) & 0 \\ -\sin(\theta_x) & \cos(\theta_x) & 0 \\ 0 & 0 & 1 \end{bmatrix}.$$

The transformation Q is equivalent to a rotation of the coordinates with respect to the origin. Figure 1 shows the geometrical transformation of this operation: Consider the rectangular "brick" B in the input coordinate $X-Y-Z$ space as shown in Fig. 1(a). By applying the rotation operation $R_x(\theta_x)$, the output coordinates rotate around the X_o -axis by θ_x in a counterclockwise direction. This is equivalent to rotating the brick B by θ_x in a clockwise direction in the output coordinates as shown in Fig. 1(b). Applying the operation $R_y(\theta_y)$ to the θ_x -rotated brick in Fig. 1(b) is equivalent to further rotating the coordinate along the Y_o -axis by θ_y degree(clockwise) and hence the brick actually rotate in a counterclockwise direction as shown in Fig. 1(c). Finally, applying $R_z(\theta_z)$ to the θ_y -rotated brick gives the θ_z -rotated (clockwise direction) brick as shown in Fig. 1 (d).

B. Equation of Plane in R^3

Consider next a plane in the 3-dimensional space which is defined as a vector field $D(x,y,z)$ such that

$$D = \{ D(x,y,z) \mid D U^T = r \}, \quad (2.3)$$

where U is a 3-dimensional row vector such that $U U^T = 1$ and r is a scalar constant. Here, the vector U indicates the *normal* direction of the plane D and r is the distance of D from the origin.

C. Perpendicular Projection

The perpendicular *projection* of a 3-dimensional surface S onto a plane D can be written as

$$S_p = S + (r - S U^T) U. \quad (2.4)$$

See the geometrical interpretation of this operation in Fig. 2(a). If U lies in one of the coordinates, say Z , then this transform is equivalent to replacing the corresponding component of S ,

$z(t)$, by a constant r .

D. Upper and Lower Surface Relative to Plane D

We define the *upper surface* relative to a plane D defined in (2.3) by

$$S^+ = \{ S \mid S(t) U^T - r > 0 \}. \quad (2.5)$$

We define the *lower surface* relative to plane D by

$$\{ S^- = \{ S \mid S(t) U^T - r < 0 \}. \quad (2.6)$$

E. Cross Section of Surface S on D

The cross section of a surface S on a plane D is the set of intersection points such that

$$\{ S \mid S(t) U^T - r = 0 \}. \quad (2.7)$$

However, since $S(t)$ is a function of t , we define the *forward cross section* by

$$\{ S \mid S(t) U^T - r = 0 \text{ and } \dot{S}(t) U^T > 0 \}. \quad (2.8)$$

In other words, the *forward cross section* of $S(t)$ on a plane D is the set of intersection points such that $S(t)$ crosses D from the lower surface to the upper surface for all $t > 0$. A *backward cross section* is similarly defined (See Fig. 2(b)).

3. Hardware Implementation

In this section, we discuss the key idea of our hardware implementation. Figure 3 shows a simplified block diagram of the instrument. An input time-varying vector, $S_i(t) = [x_i(t), y_i(t), z_i(t)]^T$, is scaled by three preamplifiers so that all three signals have the same order of magnitudes. This is equivalent to applying a diagonal matrix operator

$$G = \begin{bmatrix} g_x & 0 & 0 \\ 0 & g_y & 0 \\ 0 & 0 & g_z \end{bmatrix} \quad (3.1)$$

to $S_i(t)$.

A. Implementing the Rotation Operation:

Three identical 2-dimensional rotators are used to perform the operations $R_x(\theta_x)$, $R_y(\theta_y)$, and $R_z(\theta_z)$. Observe that the connections of the three 2-dimensional rotators in Fig. 3 realizes the orthogonal transformation Q in (2.2).

Hence, the output vector $S_o(t) = [x_o, y_o, z_o]^T$ of the 3-dimensional rotator enclosed by the dotted rectangle in Fig. 3 is the rotated vector of $S(t) = [x(t), y(t), z(t)]^T$. To view its projection, we simply pick 2 of the three signals. This operation is equivalent to choosing \vec{U} to be the unit vector $[1,0,0]^T$, $[0,1,0]^T$, or $[0,0,1]^T$ and then applying the perpendicular projection (2.4) to $S_o(t)$. Since $S_o(t)$ can be rotated by any desired angle, the projection of $S(t)$ from any direction can be displayed on the oscilloscope screen.

B. Implementing the Cross Section Operation:

The three sample-and-hold (S&H) circuits and the comparator on the right hand side of Fig. 3 are all that is needed for displaying any desired cross section on D . Again, without loss of generality, we specify our plane D by choosing U in (2.3) to be the unit vector $[1,0,0]^T$, $[0,1,0]^T$, or $[0,0,1]^T$. Here, the plane D can be defined, with the help of a switch S_D , in terms of either the input coordinates (X, Y, Z) , or the output (rotated) coordinates (X_o, Y_o, Z_o) †.

†The switch S_D in Fig. 3 is drawn for the case $U = [0,0,1]^T$ for convenience. For increased flexibility and operational convenience, a 6-position switch, (3 for input coordinates, and 3 for output coordinates) is recommended.

Since U has only one nonzero element, the times when $S(t)$ intersects D can be easily and accurately detected by comparing one of the signals, say $Z(t)$, and a constant r . Since signals are time-varying, their values at the intersection point should be held for a short period of time. Three sampled-and-hold circuits are used for this purpose.

Most of the functional blocks in Fig. 3 are implemented by using off-the-shelf integrated circuit modules [10-12]. Since the detailed circuit for the design depend on the choice of integrated circuit modules, it is given in the Appendix. Readers interested in duplicating our instrument are therefore referred to the Appendix for more details.

C. Detailed Rotation Circuits:

The heart of any rotation circuit for implementing the transformation (2.2) is a *multiplier*. Although the signals to be rotated are generally changing rapidly in time, the rotation angle is either a constant, or changing continuously but slowly if we want the surfaces to be rotated *continuously* through all angles. Hence, it is possible to build a multiplier by operational amplifiers and potentiometers where the position of the potentiometers represent each element value of matrix M . If we adjust the potentiometers so that the matrix M becomes orthogonal, then M implements a rotation. This simple design, however, is inaccurate and cumbersome in practice because the adjustments are tedious and error prone.

In our design, we use a multiplying digital-to-analog converter (MDAC) as the basic multiplier. MDAC is a resistor array with electronically controllable switches (for example, MOS transistors). Hence, it can be used either as a multiplier, or as a variable-gain amplifier when incorporated with a summing operational amplifier. Eight- to twelve-bit MDACs[10,12] are now widely available.

Figure 4 shows detailed circuit diagram of this scalar multiplier using an MDAC[12]. Here, an eight-bit $R-2R$ ladder network generates a set of binary-weighted currents. Digitally controlled switches, $S-1$ to $S-8$, are used to switch these currents between the ground and the operational amplifier input which is at virtual ground. Since these currents are proportional to

the input voltage V_i , the output voltage is given by

$$V_o = - \left(\frac{D_7}{2^1} + \frac{D_6}{2^2} + \dots + \frac{D_0}{2^8} \right) V_i \quad (3.2)$$

where $D_n = 1$ or 0 .

Hence, the *gain* between the input and the output varies from $\frac{0}{256}$ to $\frac{255}{256}$. This means that the multiplier constant can be adjusted to any value between 0.0 to 1.0, and accurate to within the discretization error.

Figure 5 is the circuit diagram for a 2-dimensional matrix multiplier consisting of four scalar multipliers m_1 , m_2 , m_3 , and m_4 . The two operational amplifiers are connected as adders to implement the summing operation required in the matrix multiplication. The relation between the inputs and the outputs of this circuit is

$$\begin{bmatrix} x_o \\ y_o \end{bmatrix} = \begin{bmatrix} r_{11} & r_{12} \\ r_{21} & r_{22} \end{bmatrix} \begin{bmatrix} x_i \\ y_i \end{bmatrix} \quad (3.3)$$

where r_{ij} can assume one of 512 discrete values between -1.0 to 1.0.

Conversion from a rotation angle θ to the multiplication constants r_{ij} can be implemented by either using a micro computer or other digital circuit techniques. In our design, a Read-Only Memory (ROM) is used to map θ into r_{ij} (See appendix for detailed discussion). This approach is both simple and efficient because it is equivalent to looking up a trigonometric function table electronically.

The mode of the sample-and-hold circuits is controlled by a comparator which detects the time t_k such that one of signals, say $Z_o(t_k)$, is equal to the reference voltage r . By holding the value of the signals at the time t_k , we can observe the intersection point on the oscilloscope screen. If the signals are sufficiently fast, the intersections, although occurring at different times, will appear to the eye as a set of points on the cross section of S on D .

The comparator output can also be used to control the beam intensity of the oscilloscope so that some part of the trajectory is blanked out from the screen. Figure 6 is an example of such a selective display. Here, $X(t)$, $Y(t)$, and $Z(t)$ are sample waveforms. If the comparator

is used to compare $Z(t)$ and the constant r , its output $C(t)$ will be as shown in Fig. 6. By applying $C(t)$ or inverted $C(t)$ to the intensity input of an oscilloscope, only the *upper* or the *lower surface* of S relative to D in (2.3) will be displayed.

Figure 7 shows an example of a cross section display. If the sample-and-hold circuits are controlled by $C(t)$, their output waveforms, $X_h(t), Y_h(t)$, and $Z_h(t)$ corresponding to the reference value r in Fig. 6 will appear as shown by the *solid* curves on Fig. 7(a), where the dotted curve denotes the original waveform. In this case, the values of $X_o(t), Y_o(t)$, and $Z_o(t)$ are held whenever $Z_o(t)$ crosses the constant value r from the upper side. Hence, if the signals during the holding periods are displayed on the screen, we would obtain a *Backward cross section* on D . In Fig. 7(b), the signals are held whenever $Z_o(t)$ crosses the constant value r from the lower side. The corresponding signals will display the *forward cross section* with respect to D .

The other circuit functions that are not shown in the block diagram in Fig. 3 include a controlling circuit for rotation angles, a reference plane generator, and a signal-reference plane multiplexer block. These blocks are included for the user's convenience.

4. Displaying Strange Attractors of a Nonautonomous Circuit

In this section, strange attractors of a second-order nonautonomous circuit will be displayed using our 3-D rotation instrument. They represent snapshots when the strange attractor S -- which is being viewed when S is rotated continuously and periodically through all angles -- is frozen momentarily at different selected angles of rotation.

Series R-L-diode Circuit

Consider the series RL-diode circuit [7-8] shown in Fig. 8(a). This circuit is similar to the one used by several other researchers except that our inductor value and the type of diode are chosen so that the strange attractor is scaled down in frequency to about 10 KHz. A 20Ω resistor is included for sensing the current I_D through the device.

As we increase the excitation frequency, we observed first a period doubling, followed period quadrupling etc., and finally a first *chaotic* band (See Fig. 14(a)). Further increase in the excitation frequency gives rise to a *period 3* periodic window. This is followed by another period-doubling process which leads to a second chaotic band, etc., as shown in Fig. 14(a).

A conventional method to characterize the periodic orbit or strange attractor in such a system is to sample the waveforms at the input frequency for different phase angles of the input signal. Such a cross section is called a *Poincare map*. Our instrument can be used not only to display these conventional *Poincare* maps, but also to look at *Poincare* maps at different perspectives. To do this, we simply choose the excitation signal as our third variable although it is not a state variable. Since the excitation signal is a periodic function of time, this third axis can be interpreted as periodically-folded map of time. Figure 8(b) shows our coordinate system for the nonautonomous case. This simple set up provides us with an extremely flexible and powerful tool for analyzing the fine geometrical structure of strange attractors that was not possible before.

Since we now have a 3-dimensional space V_D, I_D , and V_S , instead of just V_D and I_D in the conventional case, we can define a cutting plane in any desired position in the 3-

dimensional space. One advantage of this approach is that by observing the 3-dimensional surface S from only a few appropriate directions, the local structure of S can usually be determined without taking discrete *Poincare* maps at many phases of the input signal. In the special case when our cutting plane is chosen to be orthogonal to the excitation axis, then the cross section becomes the conventional *Poincare* map. In other words, our instrument is much more versatile than just taking *Poincare* maps.

The following features of our instrument are used in displaying the strange attractors in this paper:

- 1) *Prescaling* : Before applying any rotation, we always scale the input signals $S_i(t) = [x_i(t), y_i(t), z_i(t)]^T$ so that the input signals of the rotator $S(t) = [x(t), y(t), z(t)]^T$ have almost the same magnitudes.
- 2) *Projection* : Our instrument allows us to choose X_o-Y_o , Y_o-Z_o , or Z_o-X_o planes as the projection plane. Hence, for each rotation operation prescribed by $(\theta_x, \theta_y, \theta_z)$, three orthogonal projections can be taken easily.
- 3) *Cross Section* : Our instrument allows us to choose either the output (i.e., rotated) X_o-Y_o plane, or the input (i.e., unrotated) $X-Y$ plane as our cutting plane D . Moreover, either forward or backward cross section relative to D can be displayed with equal ease.
- 4) *Reference plane* : As a frame of reference to remind us of the relative position of the projection plane and the input (unrotated) $X-Y$ plane, -- henceforth called the *reference plane* --, which need not coincide with the cutting plane D , this reference plane can be displayed simultaneously with the projected surface S or the cross section. The first quadrant of this reference plane will always appear (when requested) as a *uniform grid of points* on the oscilloscope screen.

A. Projecting Periodic Attractors:

The periodic waveforms $I_D(t)$, $V_D(t)$, and $V_S(t)$ (at a fixed input frequency) are displayed in Fig. 9(a) along with the signal $C(t)$ from the comparator. Note that the period of $V_D(t)$ is 3

times that of $V_S(t)$. The projection of the surface S generated by I_D, V_D , and V_S onto the V_D-I_D plane is shown in Fig. 9(b). Note the "barely visible" 3-loop Lissajous figure indicates a period 3 relation between V_D and I_D . Here, the output signal is at the input of the sample-and-hold circuits and hence $C(t)$ is irrelevant. In figure 10, we apply the rotation operation ($\theta_x = -50.6^\circ$, $\theta_y = -18.3^\circ$, and $\theta_z = 166.0^\circ$) and then take projections. Figure 10(a) shows the position of the rotated V_D-I_D plane. The cutting plane D in this case is a plane parallel to the reference plane but passing through the V_S -axis at $V_S = r$. By comparing the waveform of $V_S(t)$ and the threshold r , we can display either the projection of the upper or lower surface, respectively.

Figure 10(b) shows the projection of the rotated Surface S onto the X_o-Y_o plane (the oscilloscope screen), along with the position of the rotated reference plane. Note the period-3 nature of $V_D(t)$ is *much clearer* than that of Fig. 9(b). This demonstrates the power of rotation provided by this instrument: with an appropriate choice of rotation angles ($\theta_x, \theta_y, \theta_z$), the projection reveals much more details of the attractor that were otherwise hidden (as in Fig. 9(b)) prior to rotation.

In addition to the projection shown in Fig. 10(b), where the comparator signal $C(t)$ is irrelevant, Fig. 10(c) and (d) show the projection of the *upper* and *lower* surface achieved by blanking out the other portion with the help of the blanking signal $C(t)$. Note that if we superimpose Fig. 10(d) on Fig. 10(c), we would recover complete projection in Fig. 10(b), as expected.

As a second application of the comparator signal $C(t)$, we use it to display the *backward* and *forward* cross sections of the above period-3 attractor relative to the cutting plane D through $V_S = r$, as depicted in Fig. 11(a). The signal $I_D(t), V_D(t)$ and $V_S(t)$ at the output of the sample-and-hold circuits are shown in Fig. 11(b) along with $C(t)$. As expected, the backward and forward cross section shown in Fig. 11(c) and (d) consist of 3 *isolated* points indicating $V_D(t)$ is period 3 relative to $V_S(t)$.

B. Projecting Chaotic Attractors:

Figures 12(a), (b), and (c) show the projection of the rotated chaotic attractor (in the first chaotic band in Fig. 14(a)) on the three orthogonal planes (X_o-Y_o , Y_o-Z_o , and Z_o-X_o planes) where the input signal V_S is a triangler waveform. Some part of this strange attractor is not clearly displayed because its probability of being visited by the chaotic signal is small relative to the other part of the attractor. However, by taking appropriate cross section views, this "exposure" problem will be overcome. The relative position of the rotated V_D-I_D plane corresponding to Fig. 12(a), (b), and (c) are depicted in Fig. 12(d).

Figure 13 shows the projection of several backward cross sections of the above strange attractor relative to the cutting plane D passing through several different values of $V_S = r$, as depicted in Fig. 13(a). Note that while the dotted reference plane in Figs. 13(b)-(f) has been rotated, our cutting plane D is always perpendicular to the vertical axis V_S .

Observe that the cross section in Fig. 13(f) reveals the presence of two "legs" (magnified in Fig. 14(b)) which was not observable from the cross sections (b),(c), and (d). This 2-leg attractor corresponds to that observed from the first chaotic band reported in [8].

Another cross section measured with the input frequency chosen to lie within the second chaotic band in Fig. 14(a) is shown in Fig. 14(c). This 3-leg attractor corresponds to a similar attractor reported in [8].

The above example clearly demonstrates the importance of choosing different cross sections, which in our instrument corresponds to tuning a single knob to set the dc reference signal r .

5. Displaying Strange Attractors of an Autonomous Circuit

The chaotic behavior of Chua's circuit (Fig. 15) has been reported in [3,5,6]. From hundreds of hours of computer simulation the chaotic attractor was found to have cross sections consisting of two tightly wound spirals. The unique geometric structure inspires the name *double scroll*. No one, however, has seen the double scroll cross section experimentally. One of our objectives in this section is to confirm the double scroll structure using our 3-D rotation instrument.

The waveforms of the three state variables, $-I_L$, V_{C1} and V_{C2} are shown in Fig. 16, where the horizontal scale is 1 msec / div. Note that all variables oscillate at an approximate rate of 10 KHz and that the waveforms appear to be chaotic.

A. Projection Views of the Double Scroll Attractor

Figures 17(a),(b) and (c) show the "unrotated" projection of the double scroll onto the $(-I_L) - V_{C1}$, $(-I_L) - V_{C2}$, and the $V_{C1} - V_{C2}$ planes, respectively. Figure 18(a),(b), and (c) show the projections of the rotated upper surface relative to a $Z = 0$ plane (the reference plane in this case coincides with the $Z = 0$ plane) onto the $X_o - Y_o$, $X_o - Z_o$, and $Z_o - Y_o$ planes, respectively. The relative position of the reference plane is depicted in Fig. 18(d). The "upper surface" of the double scroll shown in Fig. 18 corresponds to the portion of the double scroll above $V_{C2}=0$. Note that the "dotted" reference plane is absent from Fig. 18(c) because it is perpendicular to the paper and hence its projection consists of only points along with the 135° -straight line through the origin.

B. Cross Section Views of the Double Scroll Attractor

A cutting plane D parallel to the $(-I_L) - V_{C2}$ plane and located at $V_{C1} = r$ is shown in Fig. 19(a). Several cross sections of the double scroll on D for different values of r are shown in Fig. 20.

Figure 19(b) shows the projection of the double scroll and its four forward cross sections onto the $(-I_L) - V_{C1}$ plane. The four forward cross sections S1,S2,S3 and S4 appear as

horizontal lines in Fig. 19(b) because the projection plane ($(-I_L)-V_{C1}$ plane) is orthogonal to the $V_{C1} = r$ planes.

Figures 20(a),(b),(c) and (d) give the projection of the forward cross sections S1, S2, S3, and S4 onto the $(-I_L)-V_{C2}$ plane. In these pictures, a faint image of the projection of the double scroll onto the $(-I_L)-V_{C2}$ plane is also displayed to show the relative location of these cross sections and that of the double scroll. Note the near-circular contour corresponds to the projection of the lower "hole" of the double scroll attractor.

Backward cross sections of the double scroll can also be easily obtained. Both forward and backward cross sections of the double scroll on 3 different cutting planes(corresponding to S1, S2, and S3) are shown in Fig. 21. These pictures agree completely with the recent rigorous analysis of the geometric structure of the double scroll, where the lower line corresponds to the "entrance gate" and the double spiral correspond to the "exit gate" [9].

The proceeding projections and cross sections were measured directly(i.e., without rotation) from the double scroll. Figure 22 shows the result obtained by rotating the double scroll as depicted in Fig. 22(a) by an angle $\theta_r = 56.25^\circ$ about the V_{C1} -axis as depicted in Fig. 22(a). The projection of this rotated double scroll onto the X_o-V_{C1} plane is shown in Fig. 22(b) along with the two forward cross sections S1 and S2 on the cutting plane parallel to the X_o-Y_o plane and passing through $V_{C1} = r$ (See Fig. 22(a)). This projection reveals that the upper and lower Saturn-like subset of the double scroll are *extremely thin* and that they are parallel to each other and perpendicular to the X_o-V_{C1} plane. This conclusion had of course been reported in [3] and proved in [9], but not before spending literally hundreds of hours on the computer. Using our instrument, this important geometrical structure is revealed instantly.

The projection of the two forward cross sections S1 and S2 of the rotated double scroll on the cutting planes depicted in Fig. 22(a) are shown in Figs. 23(a) and (b), respectively. Note that they are merely rotations by the same angle θ_r of the corresponding cross sections in Figs. 20(a) and (b), respectively, as expected.

Our final figure 24 shows the superposition of a projection and a cross section of the double scroll after it has been rotated by some angle θ_x , θ_y , and θ_z . The cutting plane in this figure coincides with the projection plane (X_o - Y_o plane). By applying the blanking signal $C(t)$ corresponding to $r=0$, we obtain the projection onto the X_o - Y_o plane of the *upper* double scroll in Fig. 24(b), and of the *lower* double scroll in Fig. 24(c), respectively. As expected, if we join the two halves in Fig. 24(b) and (c) together, we would obtain the complete cross section in Fig. 24(a). These *half* cross sections are very useful in that they reveal the directions of the trajectories (out of the paper in Fig. 24(b) and into the paper in Fig. 24(c)) in different portions of the cross section. Such information is invaluable in deriving the fine "local" structure of strange attractors.

6. Conclusion Remarks

This paper describes the design of a real-time preprocessor for the oscilloscope for rotating a 3-dimensional Lissajous figures through any angle, either fixed at some discrete value, or varying continuously in a periodic manner. Applications of this 3-D rotation instrument for observing strange attractors are illustrated for both autonomous and non-autonomous circuits. Many of the projections and cross sections of strange attractors have never been seen before and reveal much new insights into the local structure of strange attractors. Many of these cross sections confirmed observations which were obtained previously through hundreds of hours of brute force computer simulation.

Since the rotation operation is valid not only in 3-dimension, but in any dimension, our basic design can be easily extended to any higher dimension. In particular, this extension is applicable to the measurement of higher-dimensional dynamic systems and for monitoring multiple-channel signals. Since the complexity of the geometric structure in strange attractor grows very quickly as the dimension increases, brute-force computer simulation is no longer practical. In such cases, higher-dimensional versions of this instrument would play an increasingly important if not indispensable role.

Our present instrument is built using only low-frequency inexpensive integrated circuit modules. More careful circuit design and choice of components would result in a significantly increased operating frequency range and accuracy. Also, the controlling circuit may be replaced by a micro computer or interfaced with the host controller for increased flexibility.

In addition, more flexible reference signals can be generated by using ROM and D/A converters. Our extensive applications of the instrument have shown that the reference signals are not just for convenience, but often they play crucial roles in identifying what we are looking at and their approximate scale. Hence, even though it is not essential, a reference-signal generator implementation in this instrument is highly recommended.

Also several comparators may be helpful in dividing the surface S into several regions simultaneously. This feature would certainly increase the flexibility of our measurement

process.

Finally, we can not overemphasize the invaluable applications of our 3-D rotation instrument as a tool for analyzing the geometric structures of 3-dimensional Lissajous figure in general, and of strange attractors in particular.

Acknowledgement

The authors would like to thank K. Krieg for many useful suggestions and assistance and to F. Ayrom for building the double scroll circuit.

References

- [1] J. Haag, *Oscillatory Motions*, Wadsworth International Series in Engineering, Belmont, California, 1962.
- [2] B. B. Mandelbrot, *The Fractal Geometry of Nature*, W.H. Freeman and CO. San Francisco, 1982.
- [3] T. Matsumoto, L.O. Chua, and M. Komuro, "The Double Scroll," *IEEE Trans. CAS*, vol. CAS-32, pp. 797-818, Aug. 1985.
- [4] R. H. Abraham and C.D. Shaw, *Dynamics -- The Geometry of Behavior, Part two: Chaotic Behavior*. Aerial Press, Inc., Santa Cruz, California, 1983.
- [5] T. Matsumoto, "A chaotic attractor from Chua's circuit," *IEEE Trans. CAS*, vol. CAS-31, pp. 1055-1058, Dec. 1984.
- [6] G. Q. Zhong and F. Ayrom, "Experimental confirmation of chaos from Chua's circuit," *Int. J. Circuit Theory Appl.*, vol.13, pp. 93-98, Jan. 1985.
- [7] T. Matsumoto, L.O. Chua and S. Tanaka, "Simple chaotic non-autonomous circuit," *Physical Review A*, vol.-30, no.2, pp. 1155-1157, Aug. 1984.
- [8] S. Tanaka, T. Matsumoto, and L.O. Chua, "A chaotic attractor from a 2-segment piecewise-linear non-autonomous circuit," *International Symposium on CAS*, June 5-7, 1985, Kyoto, Japan.
- [9] L.O. Chua, M. Komuro and T. Matsumoto, "The double-scroll family: A Rigorous Analysis," in preparation.
- [10] *Linear Databook*, National Semiconductor Corporation, 1983.
- [11] *The TTL Data Book for Design Engineers*, Texas Instruments Incorporated, 1976.
- [12] *CMOS 8-Bit Buffered Multiplying DAC AD7524*, Analog Devices, 1985.

APPENDIX

This appendix provides the detailed circuit implementation of our instrument. Some of the circuit diagrams may appear trivial to the electronics engineers, but are included nevertheless for the novice.

A.1) *Detailed block diagram* (Figure A-1): The block diagram in Fig. A-1 includes a reference plane generator and a multiplexer for displaying signals and the reference plane alternately. The controlling circuits for the rotators are shown in the upper part of the diagram.

A.2) *Bus structure for rotators* (Figure A-2): To control the rotators, a bus structure is used. The data bus A is shared by three rotation angle counters. Data from bus A is converted into corresponding multiplying constants by a ROM. The data from bus B supplies the multiplying constants. To control different parts of the instrument, address and controlling signals are provided to all blocks. Because of our choice of a bus structure, extensions to higher-dimensional rotators can be easily done without changing the interface.

Bus control signals

wr : write-enable when wr is false

m0 : Rotator element address(LSB)

m1 : Rotator element address(MSB)

m2 : Rotator address(LSB)

m3 : Rotator address(MSB)

bus A : rotation angles ($\theta = D \frac{\pi}{128}$)

bus B : multiplying constants ($r = \frac{D}{128} - 1.0$)

A.3) *Bus timing chart* (Figure A-3): Each counter outputs its data into bus A according to its address determined by m2 and m3. The data on bus A is converted into four multiplying constants by a ROM where address signals, m0 and m1 are used to select the

corresponding function table in the ROM. These data are placed on bus B so that the multipliers can read their multiplying constants.

A.4) *Controlling circuit and reference generator* (Figure A-4): This circuit generates the address signal, m_0, m_1, m_2 and m_4 and *write-enable* signal. It also provides a clock signal for the angle counters. Two staircase signals, X_{ref} and Y_{ref} , are available for displaying the reference plane.

A.5) *Rotation angle counter* (Figure A-5): This is an example of a rotation-angle entry circuit. This circuit may be replaced by an 8-bit switch if continuous rotation is not required.

A.6) *Function ROM* (Figure A-6): Address of the ROM is specified by D_0 to D_7 in bus A and m_0 and m_1 . Data of bus B is simply a data of the ROM memory. See actual data of ROM in Table A-1.

m_1	m_0	meaning	output data
0	0	r_{11}	$\cos(\theta)$
0	1	r_{12}	$\sin(\theta)$
1	0	r_{21}	$-\sin(\theta)$
1	1	r_{22}	$\cos(\theta)$

A.7) *Detailed 2-dimensional multiplier circuit diagram* (Figure A-7): This circuit is controlled by a through bus similar to the common micro computer interface. Address decoder may vary by application. All resistors shown in the circuit diagram should have at least 0.5 % accuracy so that multiplication is accurate enough.

A.8) *Sample-and-hold and comparator circuit* (Figure A-8): Although this circuit is very simple, consult the corresponding integrated-circuit reference to avoid unexpected effects.

FIGURE CAPTIONS

Fig. 1. Geometrical interpretation of the 3-dimensional rotation operation.

- (a) Input coordinate view of rectangular "brick" B.
- (b) Output coordinate view after applying rotation operation $R_x(\theta_x)$ to (a).
- (c) Output coordinate view after applying rotation operation $R_y(\theta_y)$ to (b).
- (d) Output coordinate view after applying rotation operation $R_z(\theta_z)$ to (c).

Fig. 2. Geometrical interpretation of the perpendicular projection and cross section operation.

The plane D is defined by a normal direction vector U and the distance of the plane D from the origin (denoted by r).

- (a) Perpendicular projection of S onto plane D .
- (b) The upper and the lower cross section of S (6 solid dots in this example) relative to the plane D .

Fig. 3. Simplified block diagram of the 3-D rotation instrument.

Fig. 4. A scalar multiplier circuit.

The gain of this circuit is determined by a set of digitally-controlled switches S-1 to S-8.

Fig. 5. Simplified 2-dimensional matrix multiplier Circuit.

Modules m_1 , m_2 , m_3 and m_4 denote scalar multipliers.

Fig. 6. Sample signals illustrating the display of the *projection* of the upper and the lower surface of S .

Here, $X_o(t)$, $Y_o(t)$, and $Z_o(t)$ are sample waveforms, $C(t)$ is a comparator output signal obtained by comparing $Z_o(t)$ with a dc signal of magnitude r , and U and L denote the

time intervals corresponding to the the upper and lower surface, respectively.

Fig. 7. Sample signals illustrating the display of the *cross section* of S in both *backward* and *forward* directions.

Solid curves denote the output waveforms of the sample-and-hold circuits.

- (a) Output waveform for displaying the backward cross section.
- (b) Output waveform for displaying the forward cross section.

Fig. 8. A driven series R-L-diode circuit.

- (a) Circuitry.
- (b) Coordinates System including the excitation signal V_S .

Fig. 9. Waveforms and their unrotated projection associated with the R-L diode circuit.

Prescaling: $X = V_D$, $Y = 3,000(\Omega) I_D$, and $Z = V_S$.

- (a) Waveforms associated with a period-three limit cycle. Horizontal scale: $20 \mu \text{ sec}$.
Vertical scale: 5 V/division .
- (b) Projection on the V_D - I_D plane. The reference plane indicates 1 V/division scale.

Fig. 10. Projection of (rotated) period-three limit cycle.

Prescaling: same as Fig. 9. Rotation : $\theta_x = -50.6^\circ$, $\theta_y = -18.3^\circ$, and $\theta_z = 166.0^\circ$.

- (a) Location of the cutting plane D in this case is a V_D - I_D plane passing through $V_S = r$ (negative value).
- (b) Projection of the whole surface onto the X_o - Y_o plane.
- (c) Projection of only the upper surface onto the X_o - Y_o plane.

- (d) Projection of only the lower surface onto the X_o - Y_o plane.

Fig. 11. Cross section of the period-three limit cycle.

Prescaling: same as Fig. 9. Rotation : same as Fig. 10.

- (a) Location of the cutting plane D in this case is a V_D - I_D plane passing through $V_S = r$ (negative value).
- (b) Waveforms of $I_D(t)$, $V_D(t)$ and $V_S(t)$ at the output of the sample-and-hold circuits in response to the comparator output signal $C(t)$. Horizontal scale: 20 μ sec. Vertical scale: 5 V/division.
- (c) Projection of the backward cross section onto the X_o - Y_o plane.
- (d) Projection of the forward cross section onto the X_o - Y_o plane.

Fig. 12. Projection of the attractor located at the first chaotic band in Fig. 14.

Prescaling: same as Fig. 9. Rotation: same as Fig.10. The input signal V_S is a 8.6 KHz triangler waveform.

- (a) Projection onto the X_o - Y_o plane.
- (b) Projection onto the Z_o - Y_o plane.
- (c) Projection onto the Z_o - X_o plane.
- (d) Location of the input coordinates. The 3 squares starting from the top left position in a clockwise direction corresponds to (a), (b) and (c), respectively.

Fig. 13. Cross section of the attractor at the first chaotic band in Fig.14.

These pictures denote cross sections of the rotated attractor in Fig. 12(a).

- (a) Location of the cutting plane D in this case is a V_D - I_D plane passing through $V_S = r$ for different negative values of r .

(b), (c),(d),(e) and (f) show the backward cross sections at $V_S = 0V, -1V, -2V -2.5V$ and $-3V$, respectively.

Fig. 14. Bifurcation tree and magnified backward cross sections.

- (a) Qualitative sketch of the bifurcation tree diagram.
- (b) Magnified version of Fig. 13(f) (cross section at the first chaotic band).
- (c) Magnified backward cross section at the second chaotic band where the input frequency is 12.0 KHz.

Fig. 15. Chua's circuit.

- (a) Circuitry.
- (b) Constitutive relation of the nonlinear resistor.

Fig. 16. Waveforms associated with the double scroll attractor.

Prescaling: $X = 2 V_{C1}, Y = -3,000(\Omega) I_L$, and $Z = 10 V_{C2}$. Horizontal scale: 1 msec/division. Vertical scale: 5 V/division.

Fig. 17. Projections of the unrotated double scroll attractor.

Prescaling: same as Fig. 16. Horizontal scale: 2 V/division. Vertical scale: 2 V/division.

- (a) Projection onto the $(-I_L)-V_{C1}$ plane.
- (b) Projection onto the $(-I_L)-V_{C2}$ plane.
- (c) Projection onto the $V_{C1}-V_{C2}$ plane.

Fig. 18. Projection of double scroll attractor after rotation.

Prescaling: same as Fig.16. Rotation : $\theta_x = -50.6^\circ$, $\theta_y = -18.3^\circ$, and $\theta_z = 166.0^\circ$. Horizontal scale: 2 V/division. Vertical scale: 2 V/division.

- (a) Projection onto the X_o - Y_o plane.
- (b) Projection onto the X_o - Z_o plane.
- (c) Projection onto the Z_o - Y_o plane.

Fig. 19. Cross section of 3-dimensional strange attractor.

Prescaling: $X = -3,000(\Omega) I_L$, $Y = 10 V_{C2}$, and $Z = 2 V_{C1}$. Horizontal scale: 2 V/division. Vertical scale: 2 V/division.

- (a) Location of the cutting plane D in this case is a $(-I_L)$ - V_{C2} plane passing through $V_{C1} = r$.
- (b) Multiple exposures showing the projection of the double scroll attractor and four forward cross sections S1, S2, S3 and S4 onto the $(-I_L)$ - V_{C1} plane.

Fig. 20. Forward cross sections of the unrotated double scroll attractor.

Prescaling: same as Fig.19. Horizontal scale: 2 V/division. Vertical scale: 2 V/division.

- (a), (b), (c) and (d) are projections of the forward cross sections S1, S2, S3 and S4 in Fig. 19(b) onto the $(-I_L)$ - V_{C2} plane, respectively.

Fig. 21. The forward and the backward cross sections of the double scroll attractor.

Prescaling: same as Fig.19. Horizontal scale: 2 V/division. Vertical scale: 2 V/division.

- (a), (b), and (d) are the forward and the backward cross sections at S1, S2 and S3 in Fig. 19(b), respectively.

Fig. 22. Projection of the double scroll attractor after a rotation around the V_{C1} -axis.

Prescaling: same as Fig.19. Rotation: $\theta_r = 56.25^\circ$. Horizontal scale: 2 V/division. Vertical scale: 2 V/division.

- (a) Rotation around the V_{C1} -axis and the location of the cutting plane D .
- (b) Projection of the double scroll attractor and two forward cross sections S1 and S2 onto the X_o - V_{C1} plane (X_o - Z_o plane).

Fig. 23. Forward cross section after a rotation around the V_{C1} -axis.

Prescaling: same as Fig.19. Rotation: $\theta_x = 56.25^\circ$. Horizontal scale: 2 V/ division. Vertical scale: 2 V/ division.

- (a) and (b) are projection of the forward cross sections S1 and S2 onto the X_o - Y_o plane, respectively.

Fig. 24. Double exposure of the double scroll attractor and a cross section:

Prescaling: same as Fig. 19.

- (a) Entire surface of the double scroll attractor along with one cross section after some rotation
- (b) The upper surface and a backward cross section.
- (c) The lower surface and a forward cross section.

Fig. A-1. Detailed block diagram of the 3-D rotation instrument.

Fig. A-2. Bus structure of the 3-D rotation instrument.

Fig. A-3. Bus Timing chart.

Fig. A-4. Angle data entry circuit.

Fig. A-5. Control circuit.

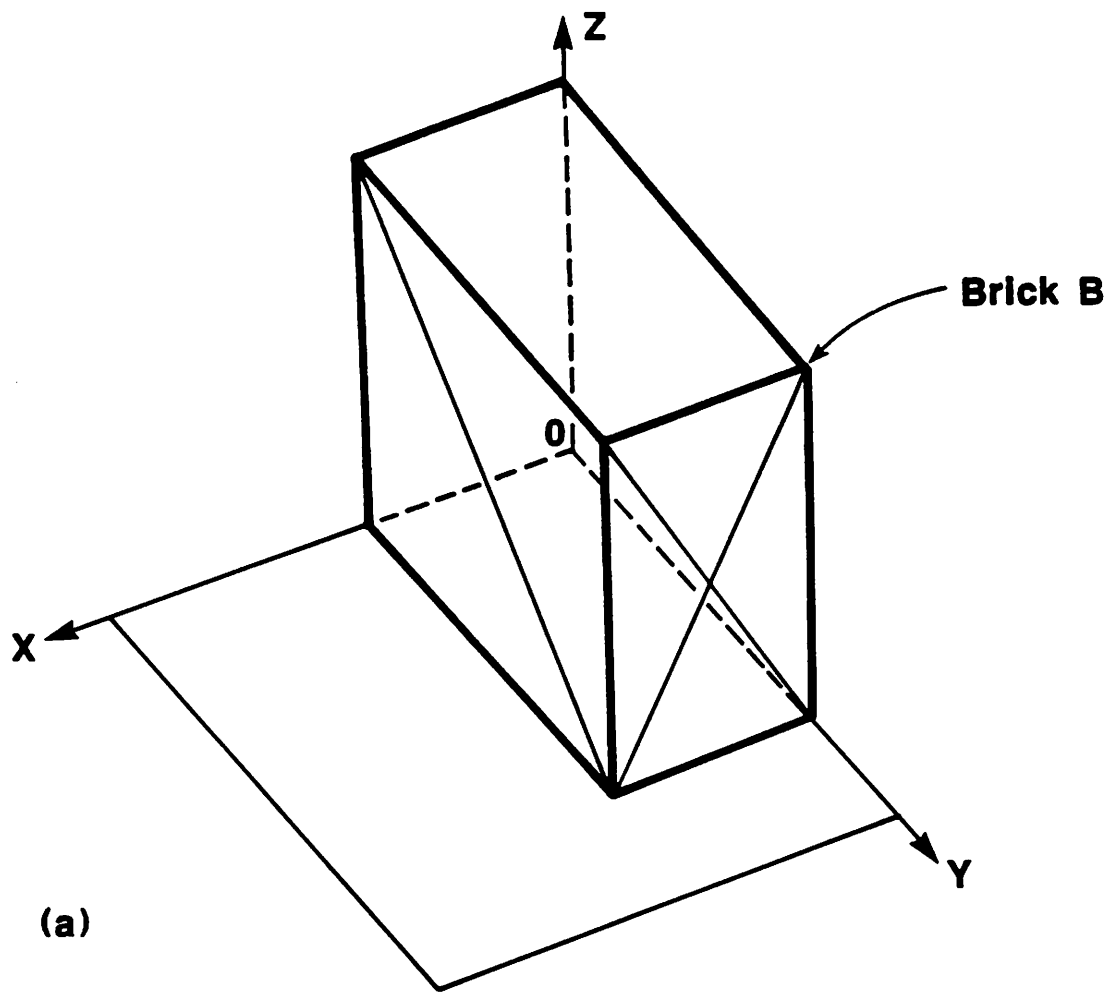
Fig. A-6. Function ROM circuit.

Fig. A-7. Two-dimensional rotator circuit.

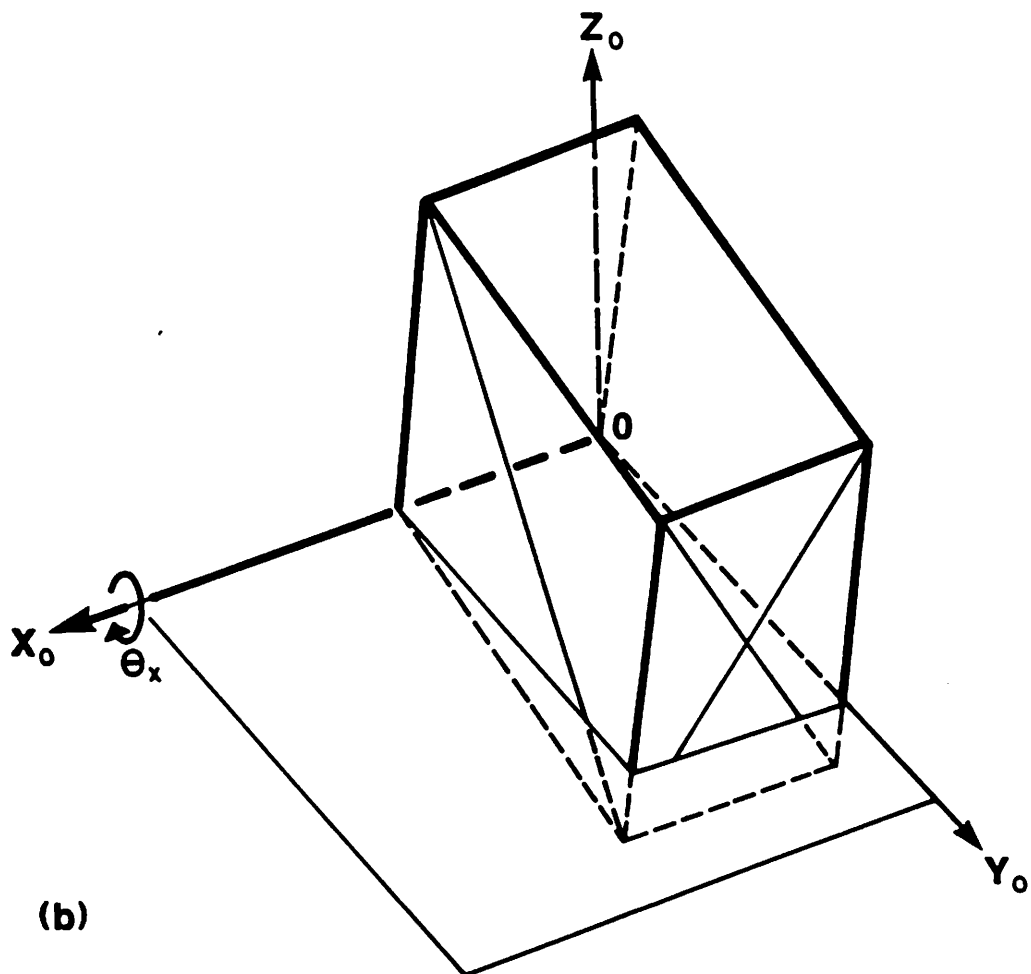
Fig. A-8. Comparator and sample-and-hold circuit.

Table A-1. Function ROM data.

The first columns are hexadecimal address of the ROM.



(a)



(b)

Fig. 1

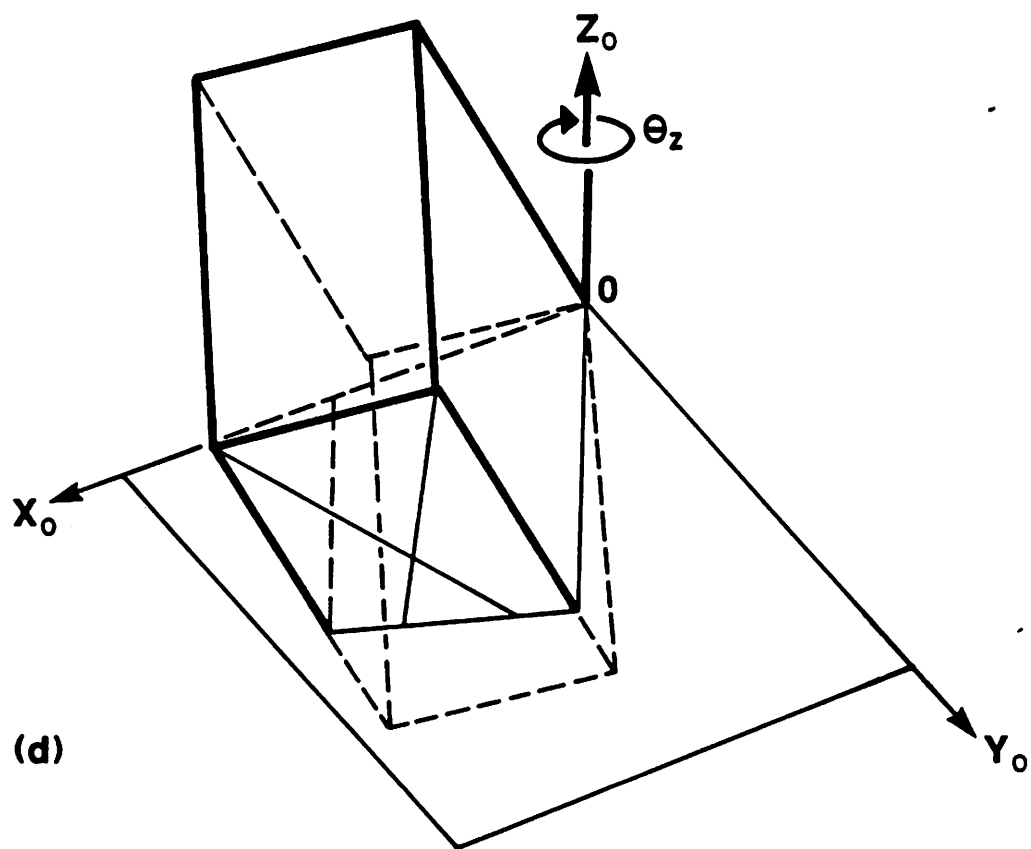
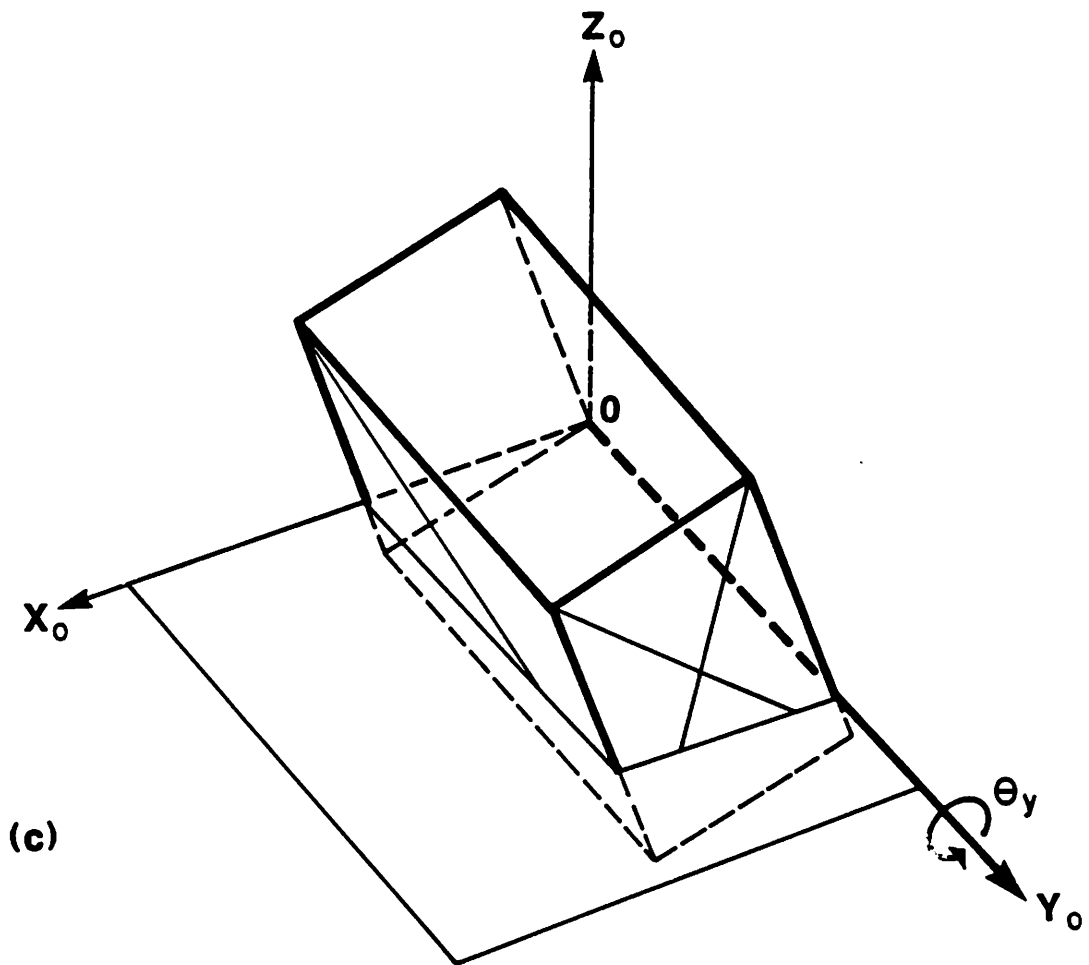
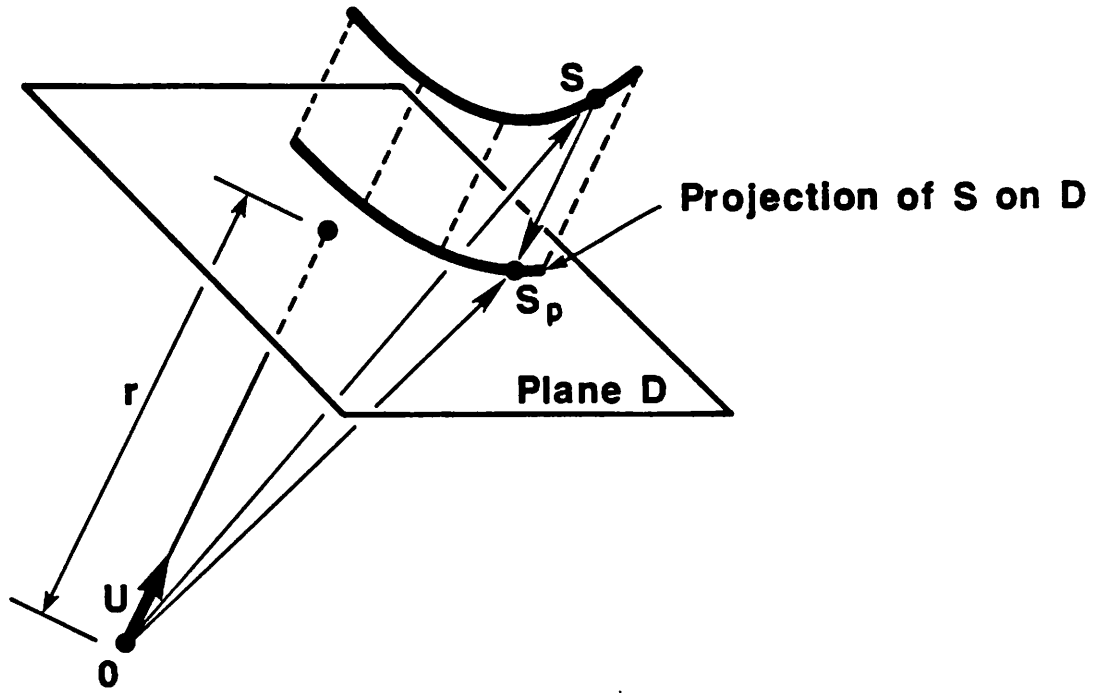
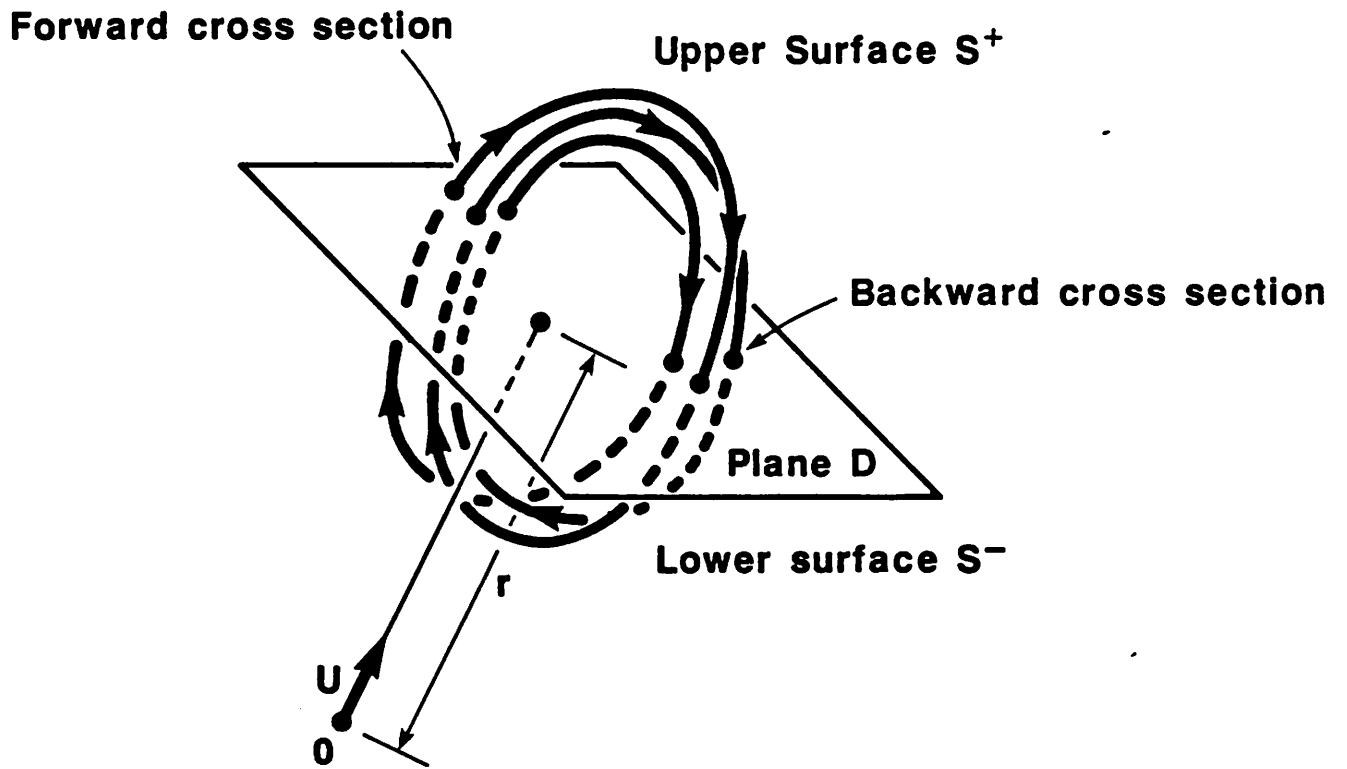


Fig. 1



(a)



(b)

Fig. 2

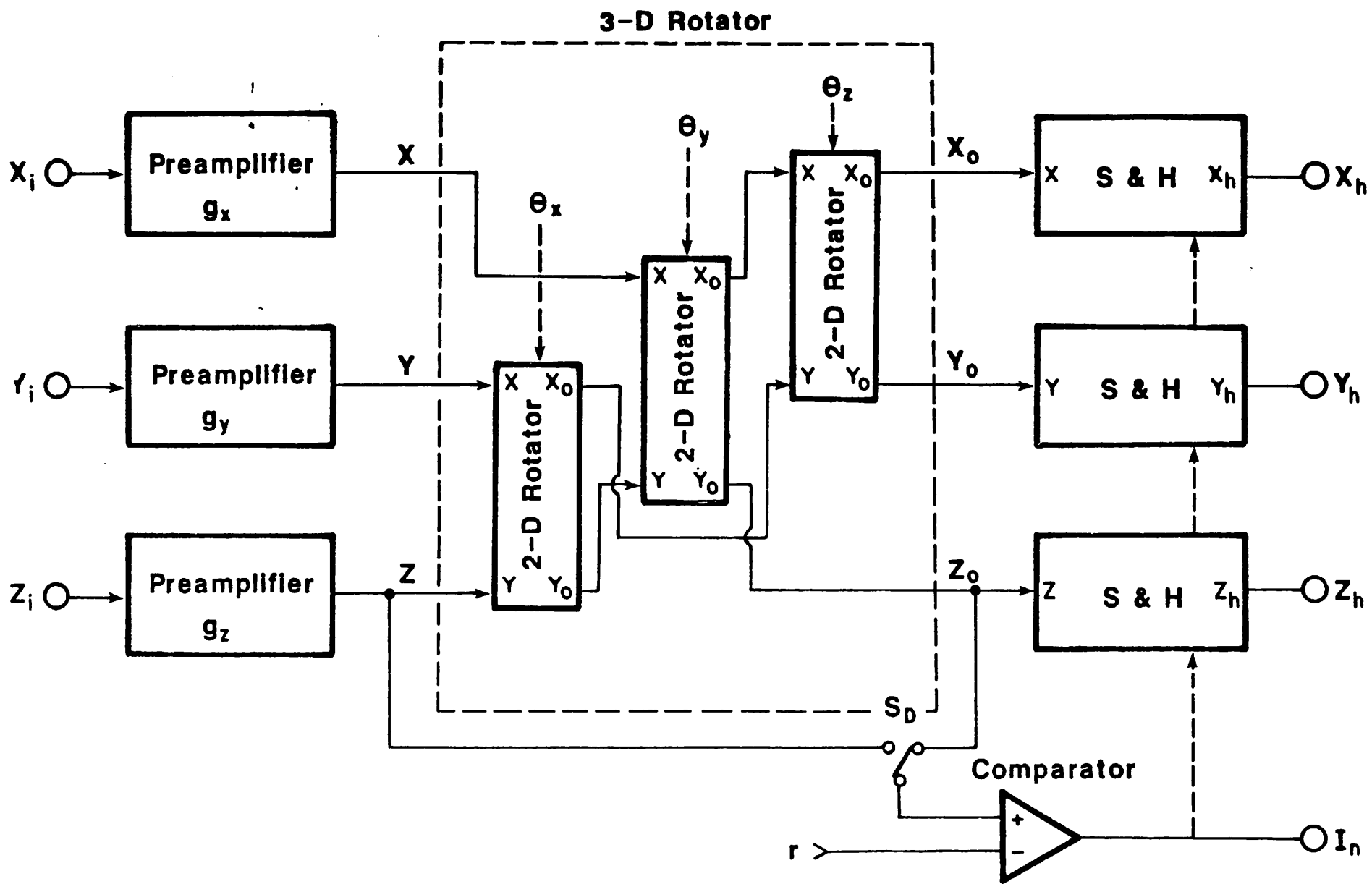


Fig. 3

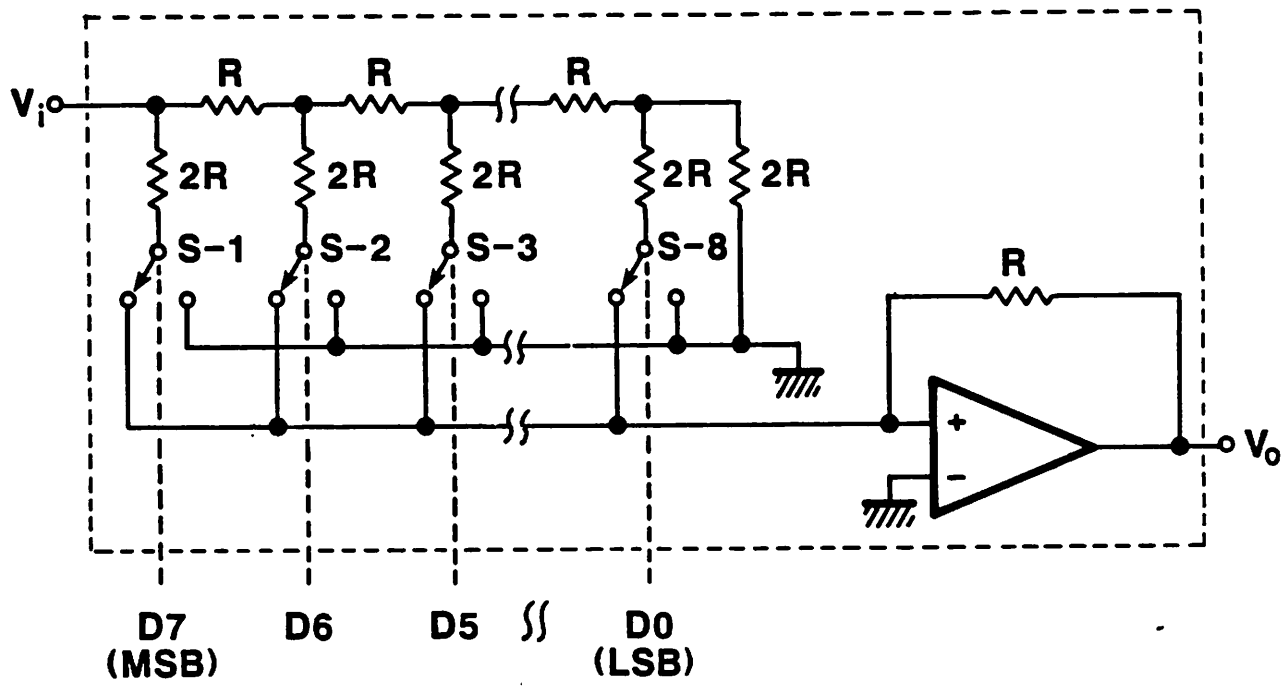


Fig. 4

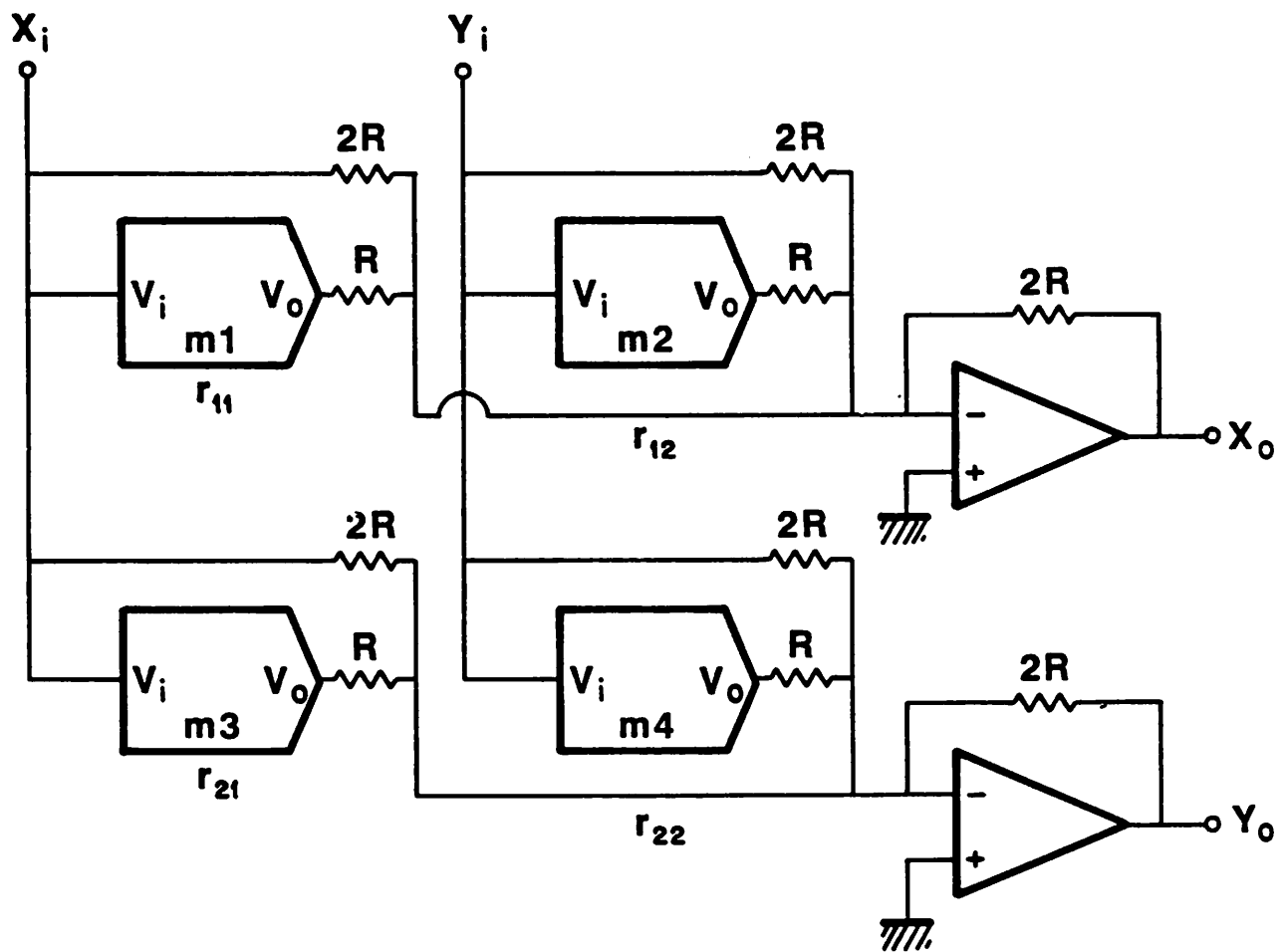


Fig. 5

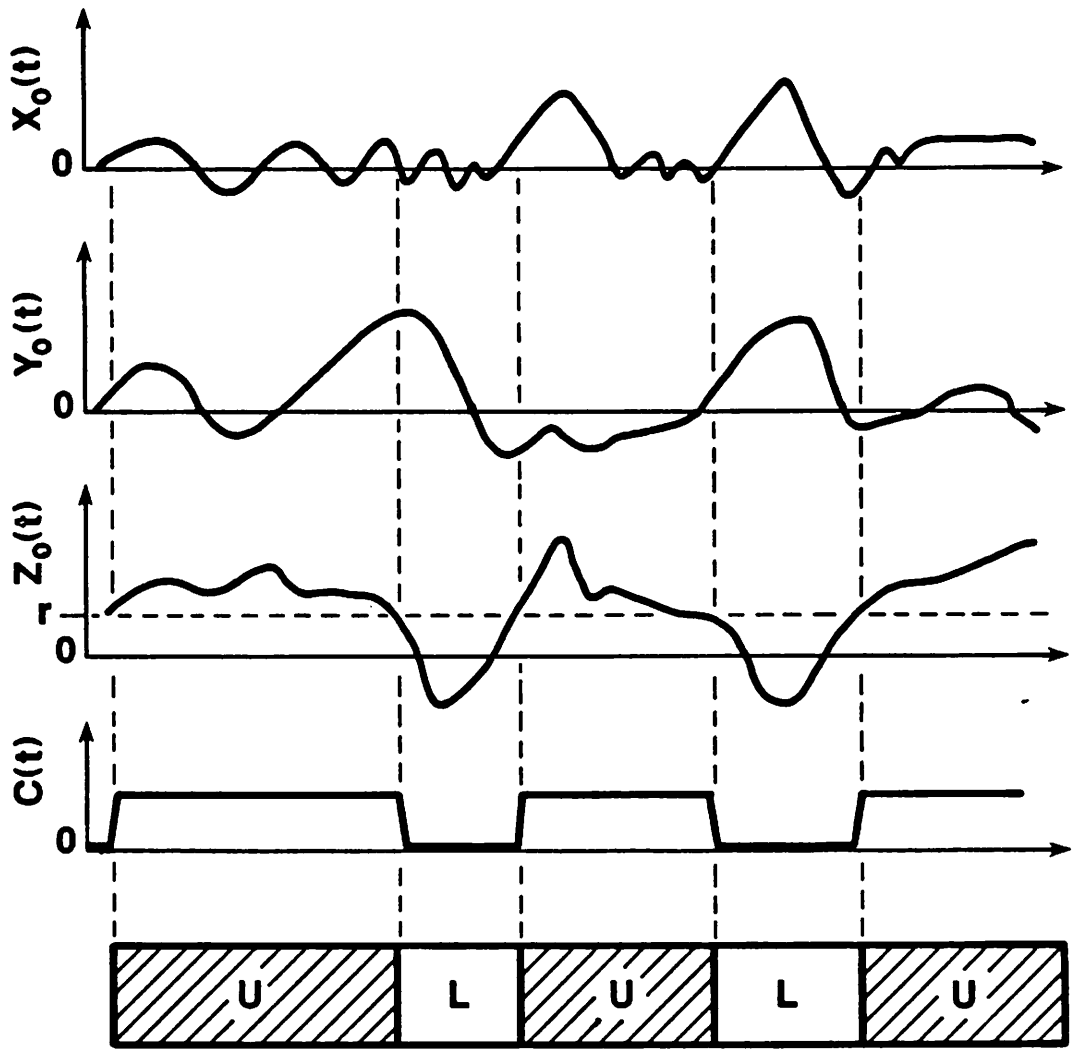


Fig. 6

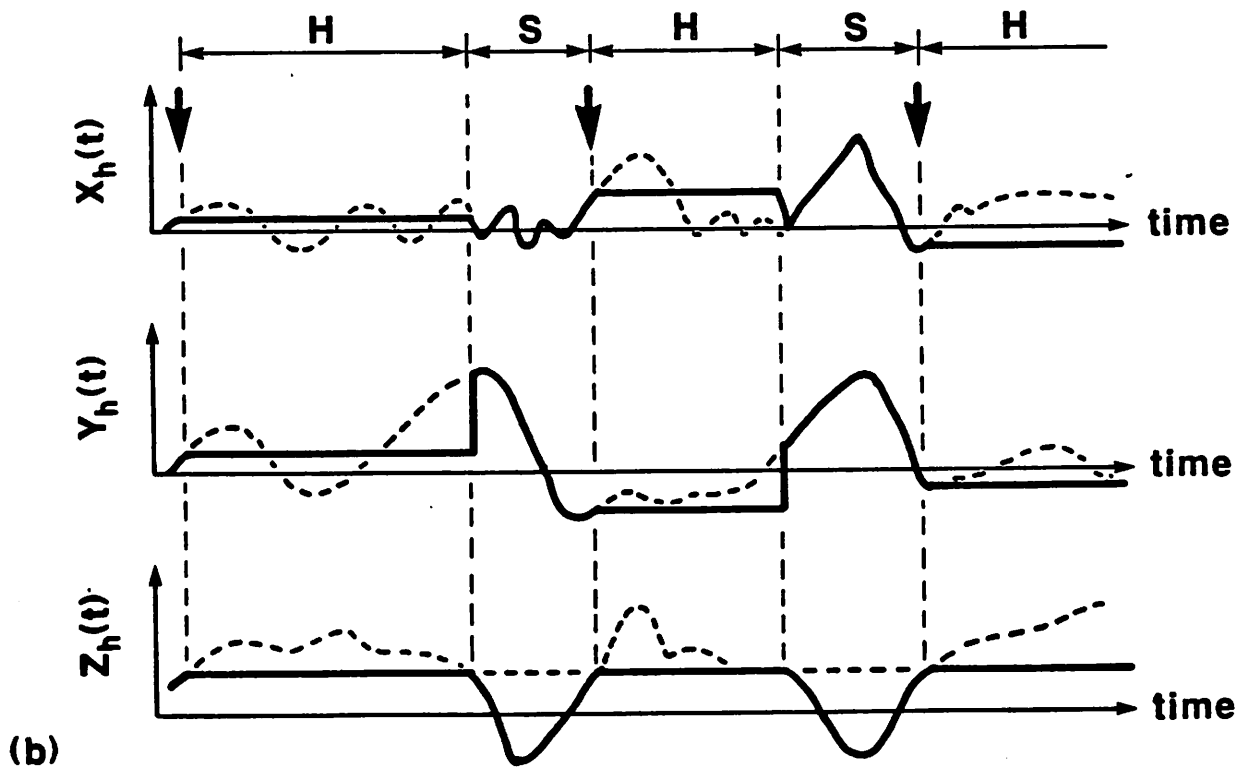
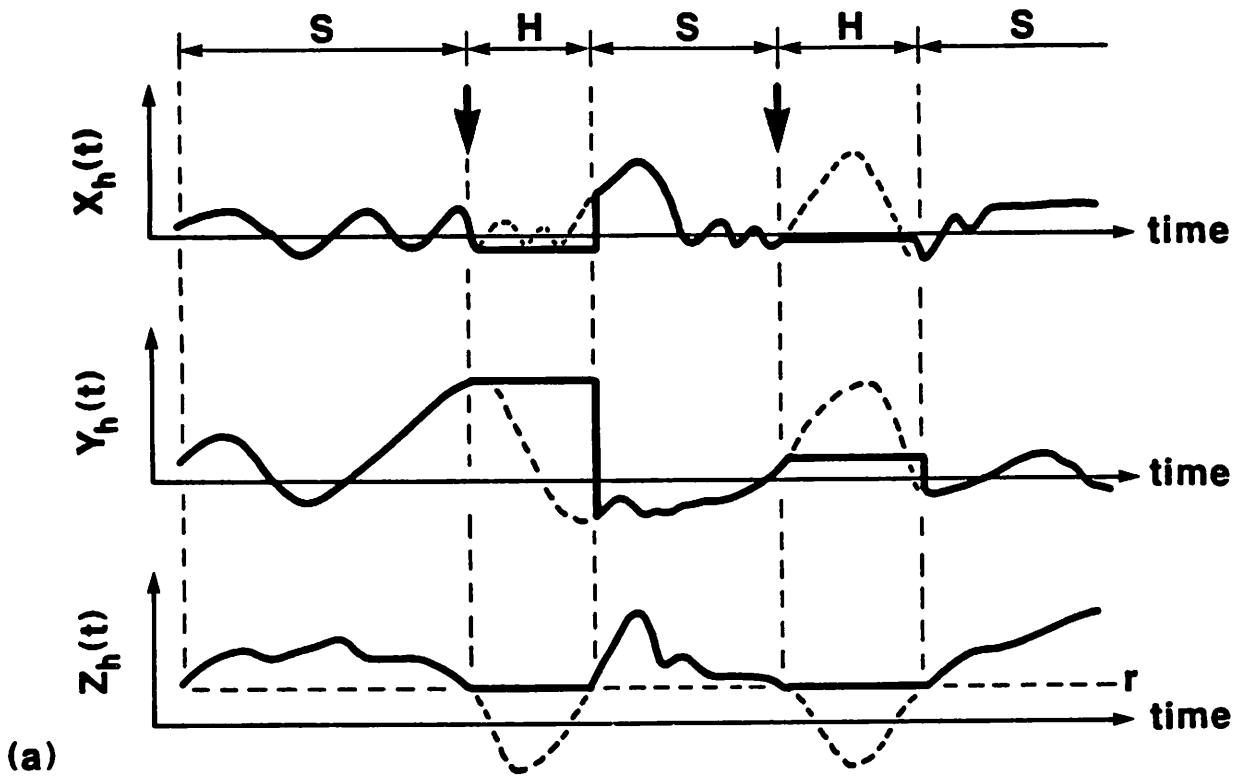
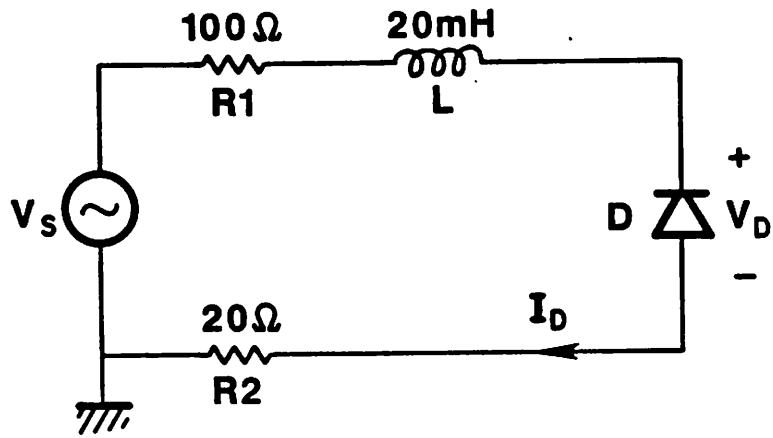
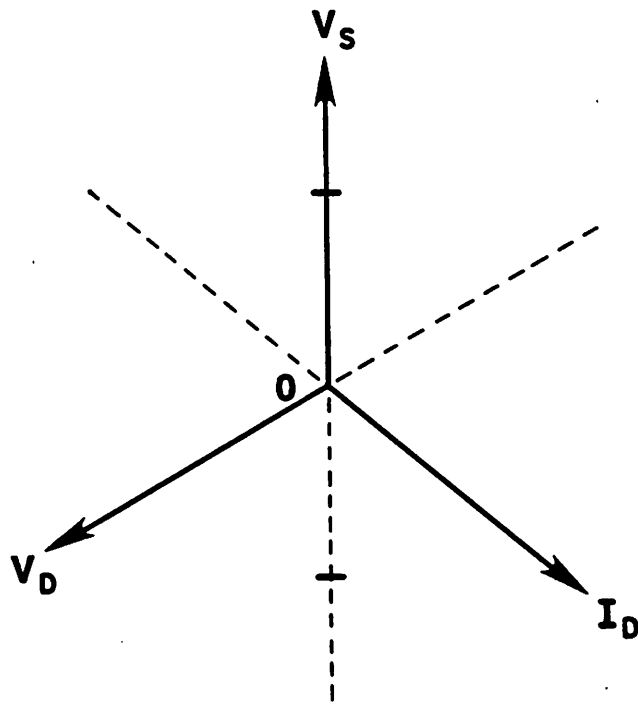


Fig. 7

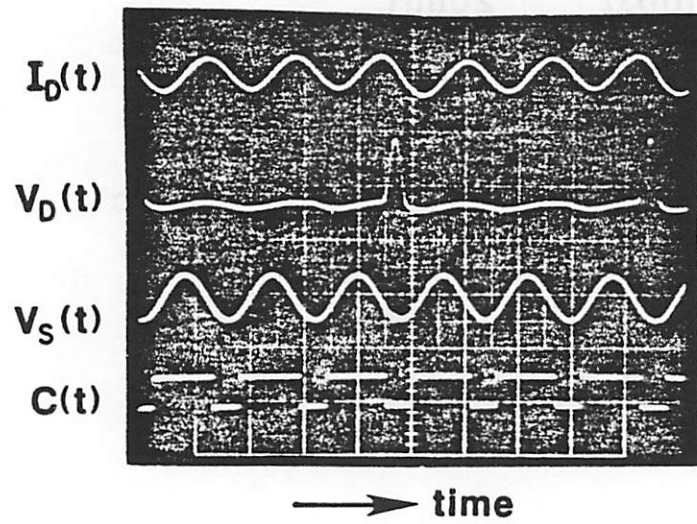


(a)

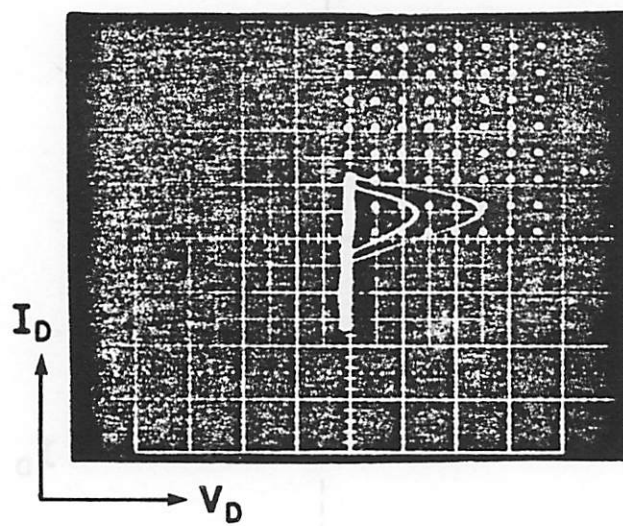


(b)

Fig. 8



(a)



(b)

Fig. 9

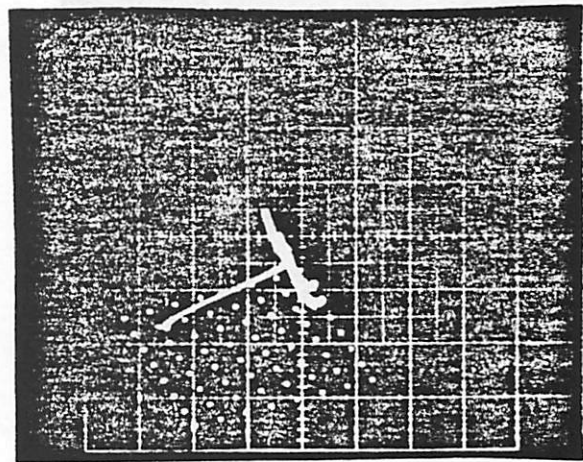
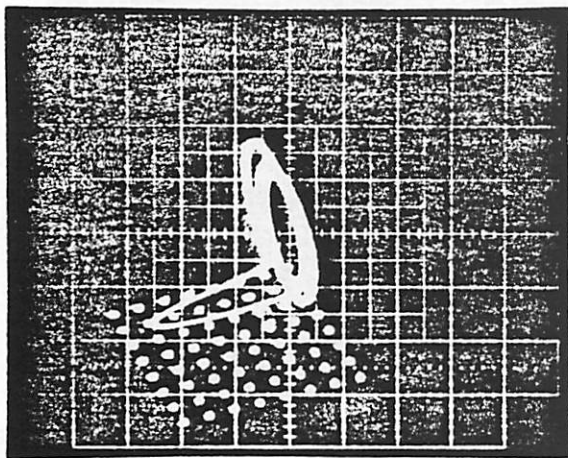
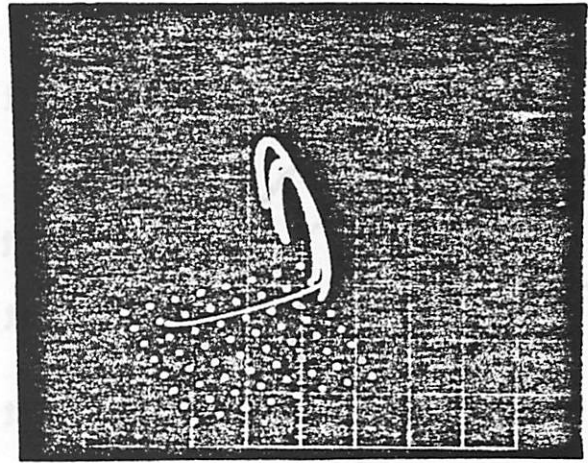
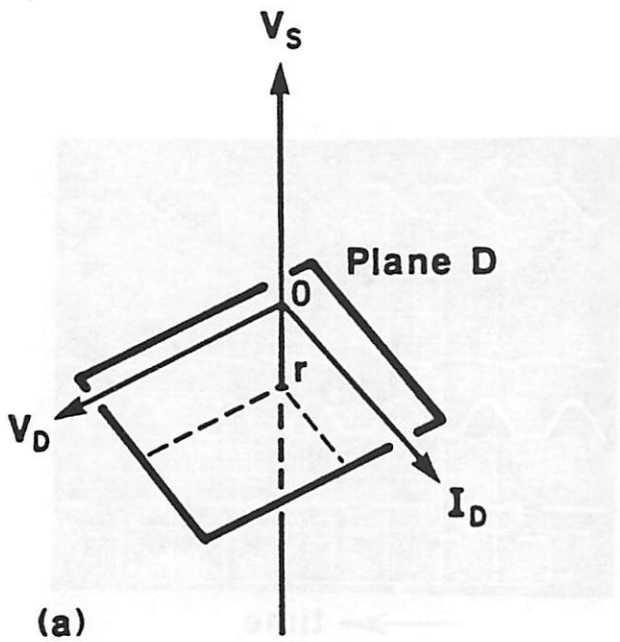
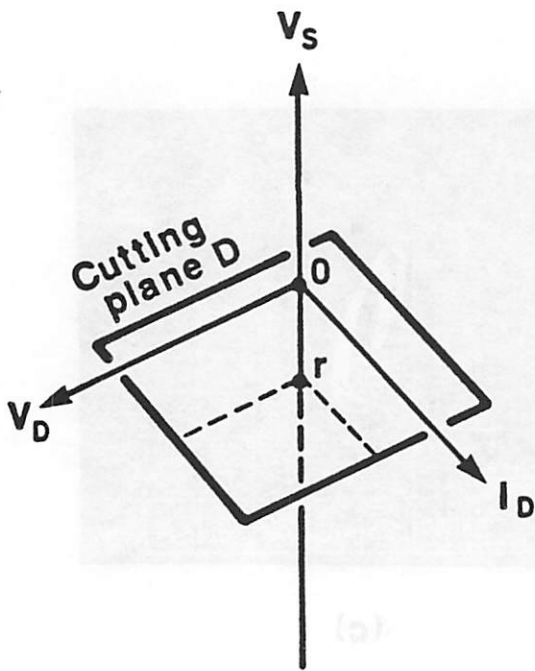
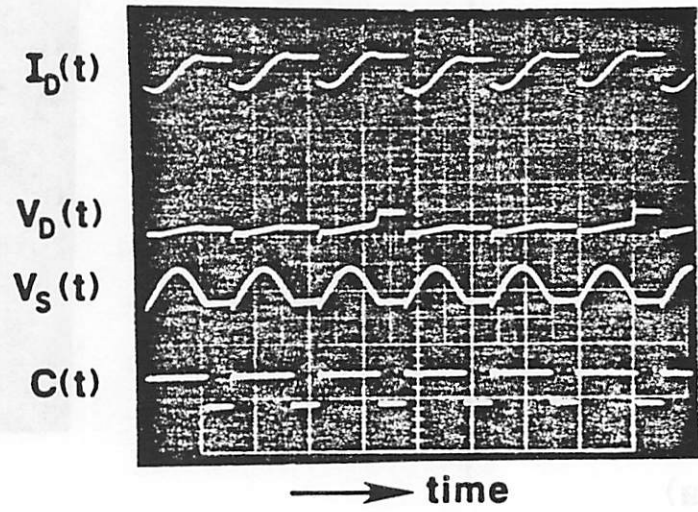


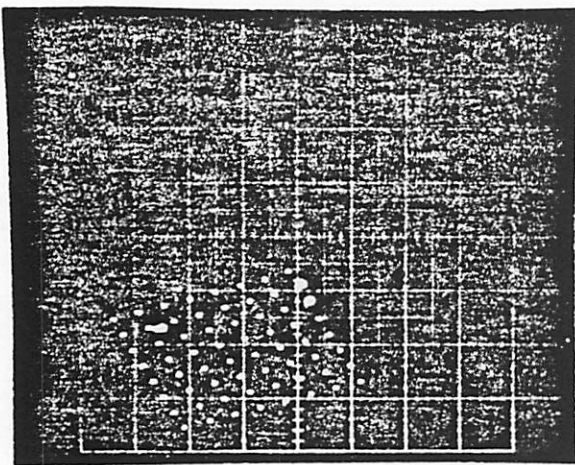
Fig. 10



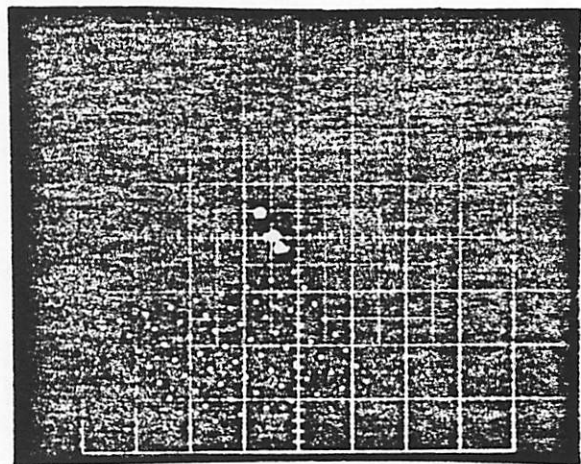
(a)



(b)

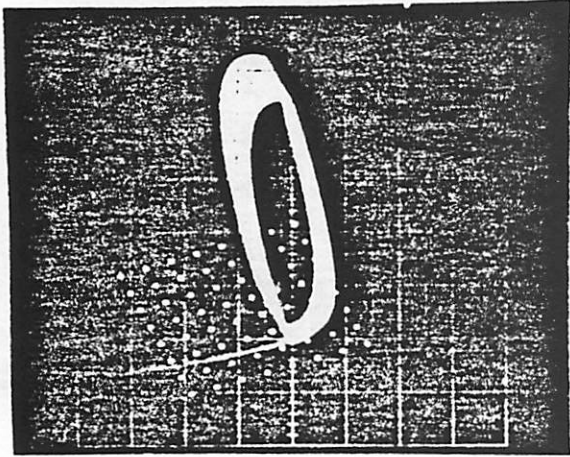


(c)

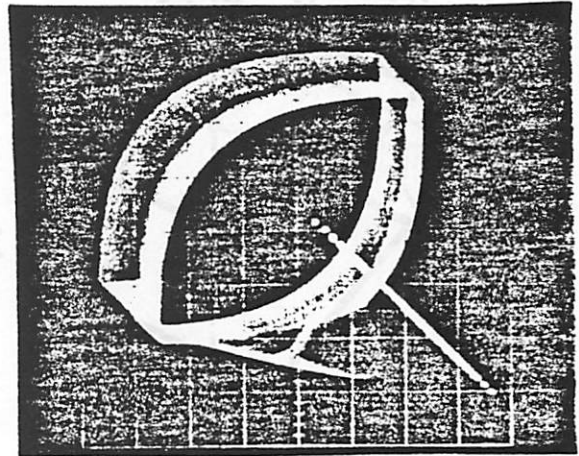


(d)

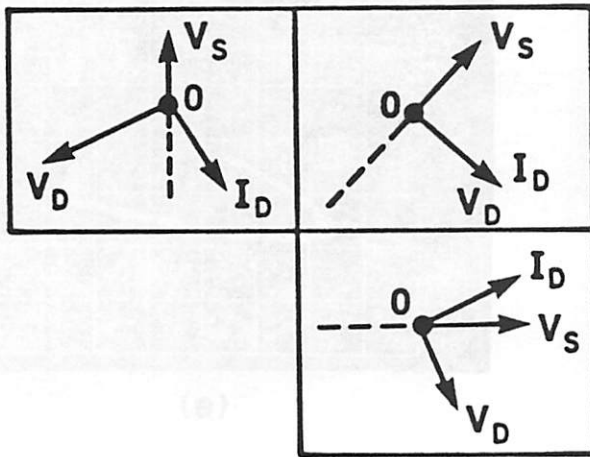
Fig. 11



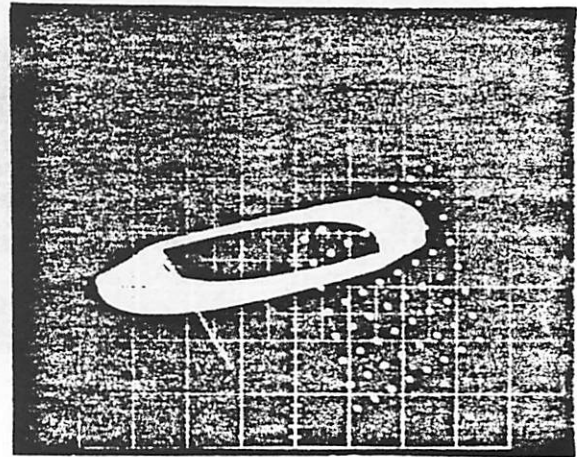
(a)



(b)



(d)



(c)

Fig. 12

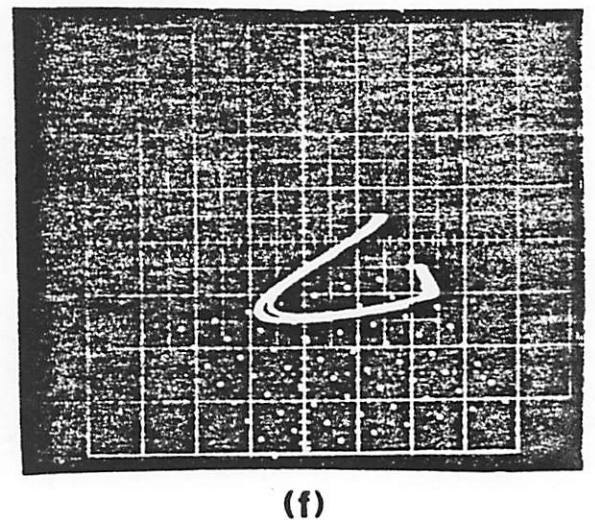
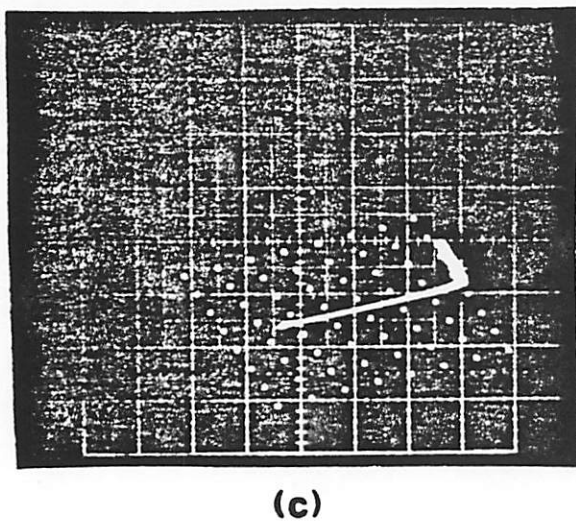
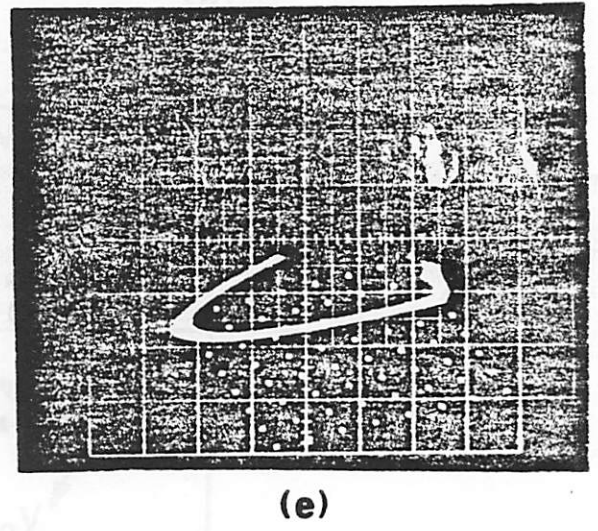
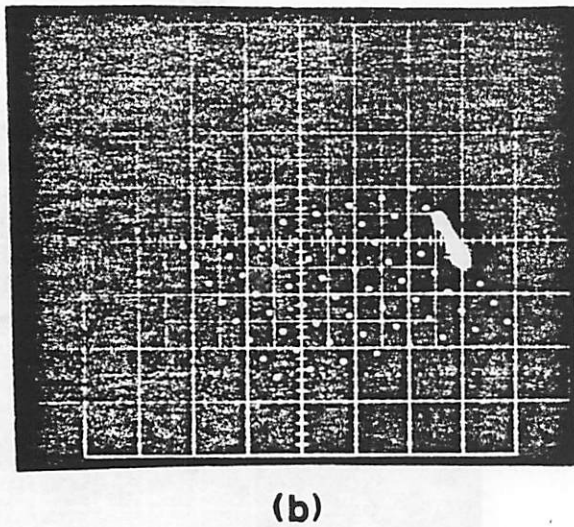
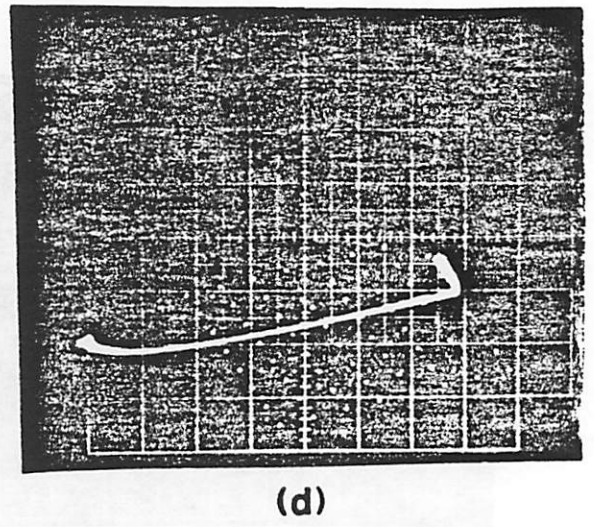
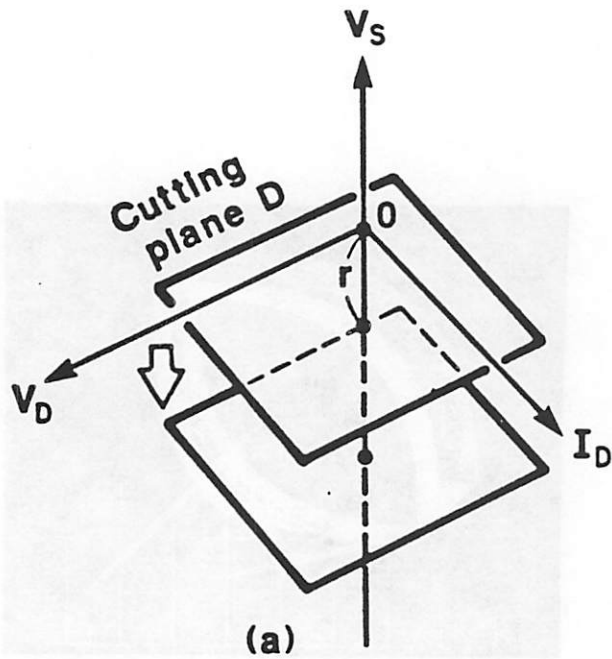
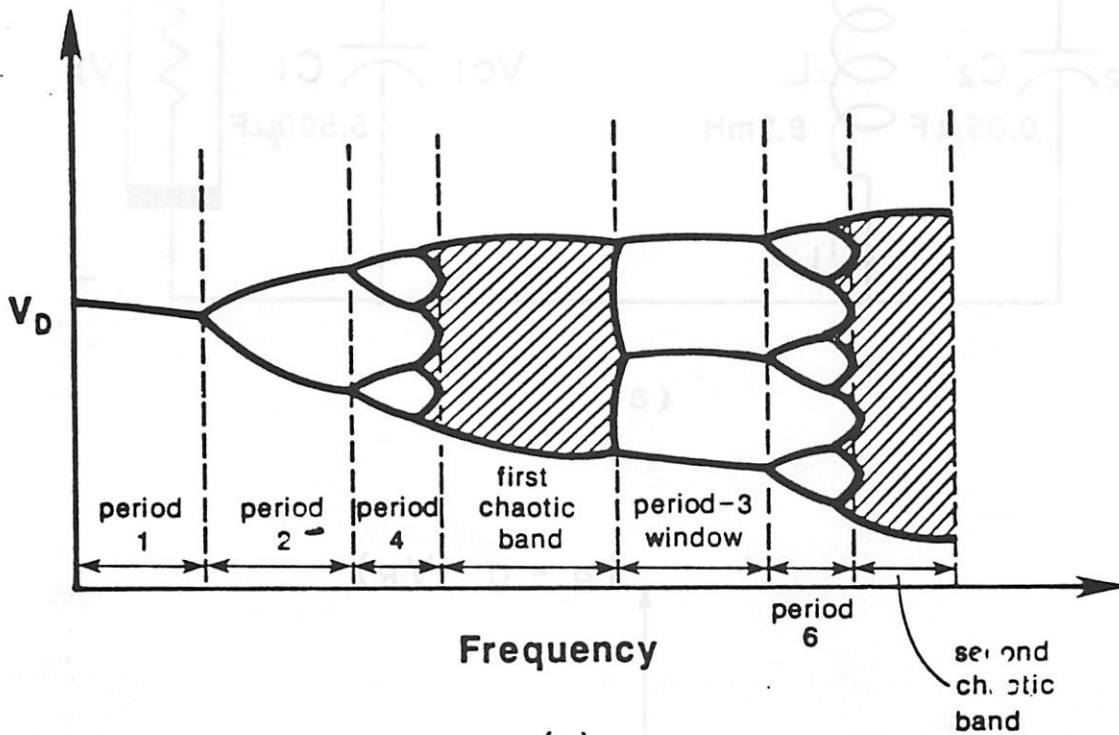
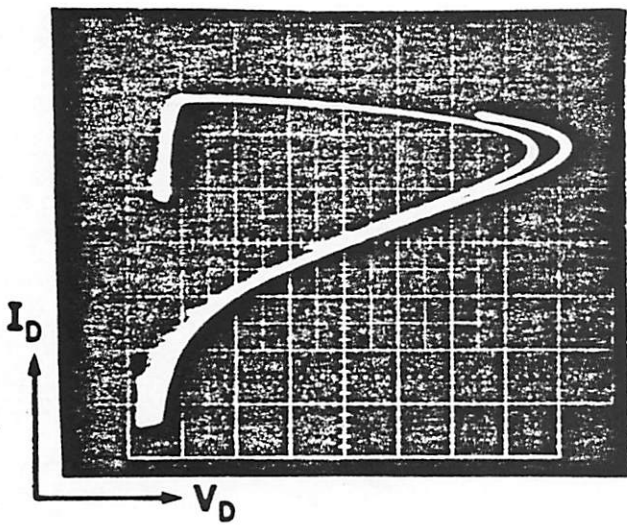


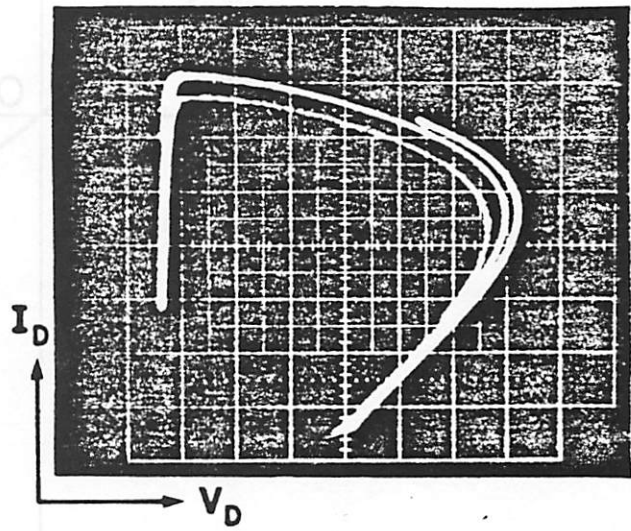
Fig. 13



(a)

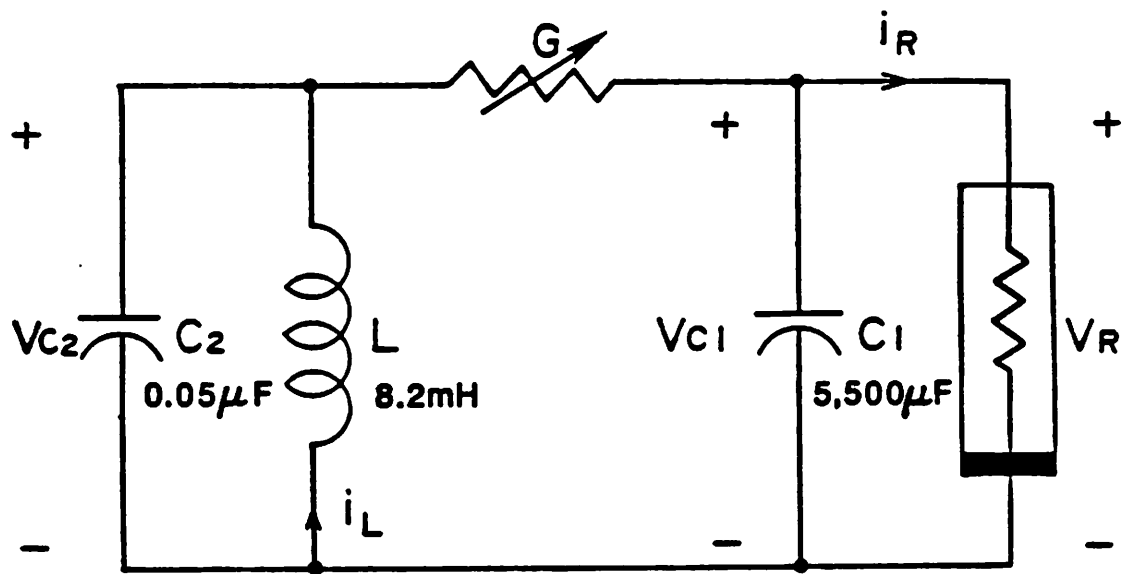


(b)

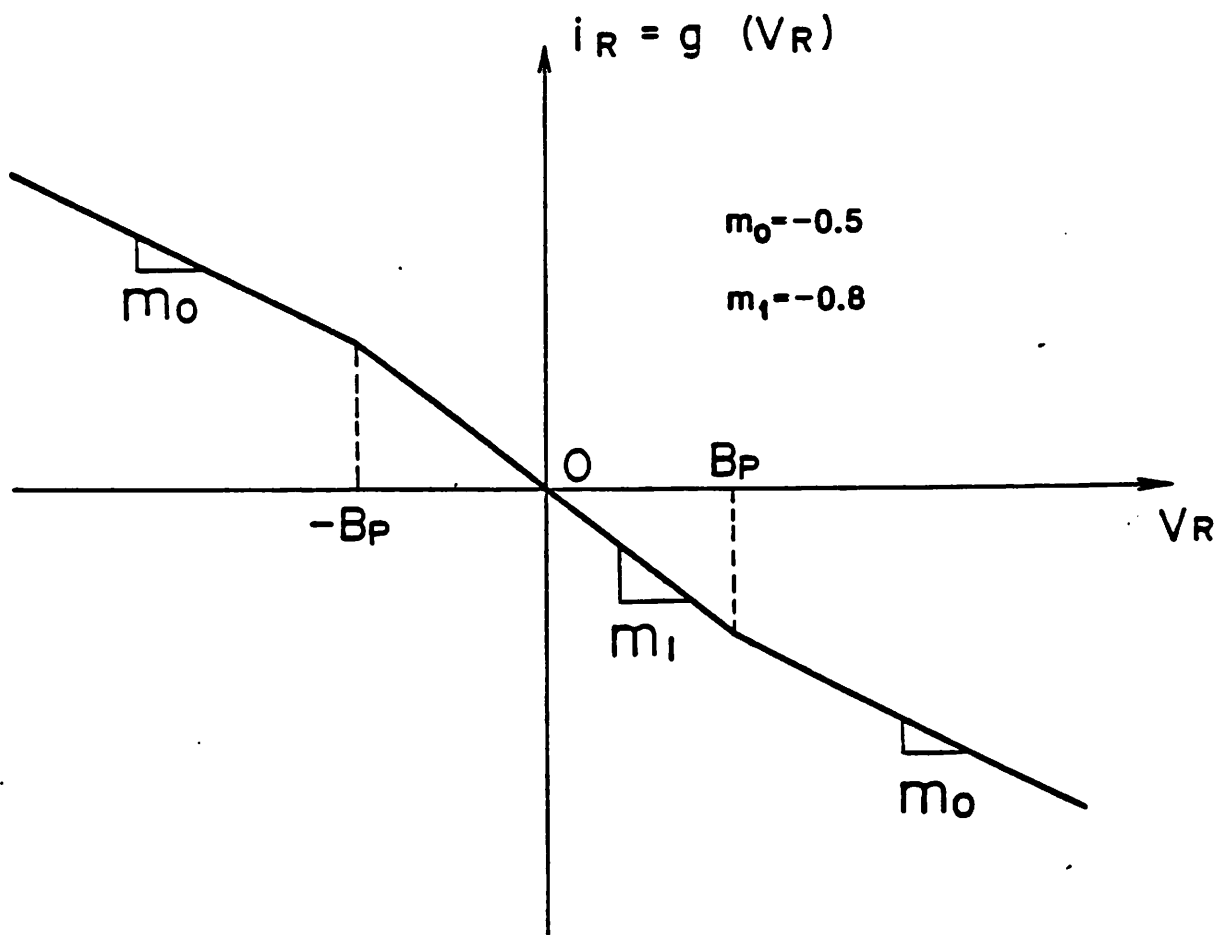


(c)

Fig. 14



(a)



(b)

Fig. 15

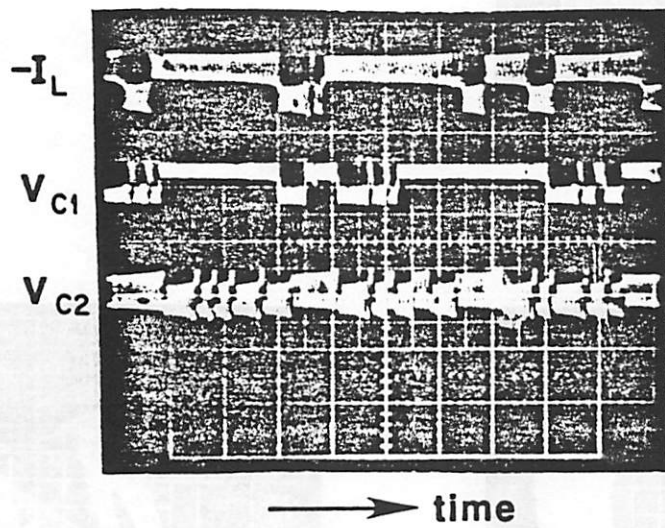
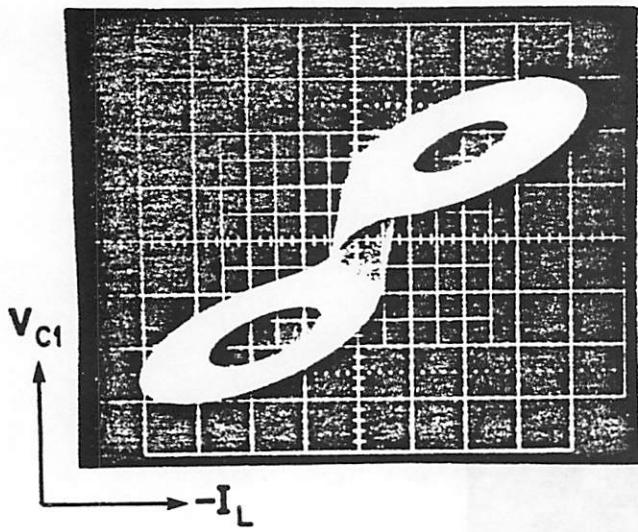
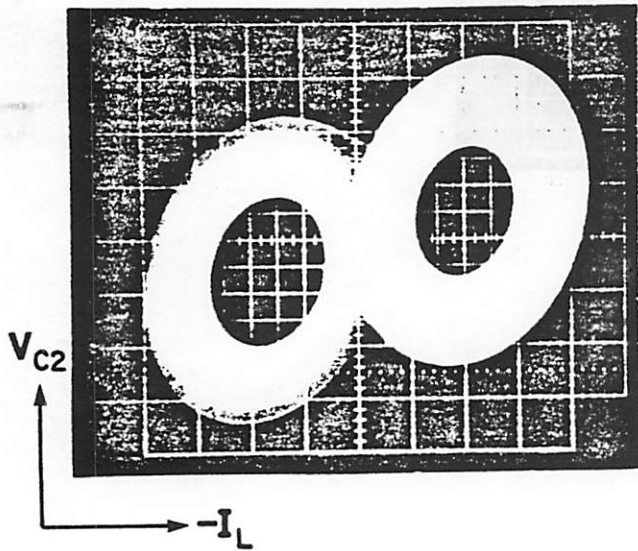


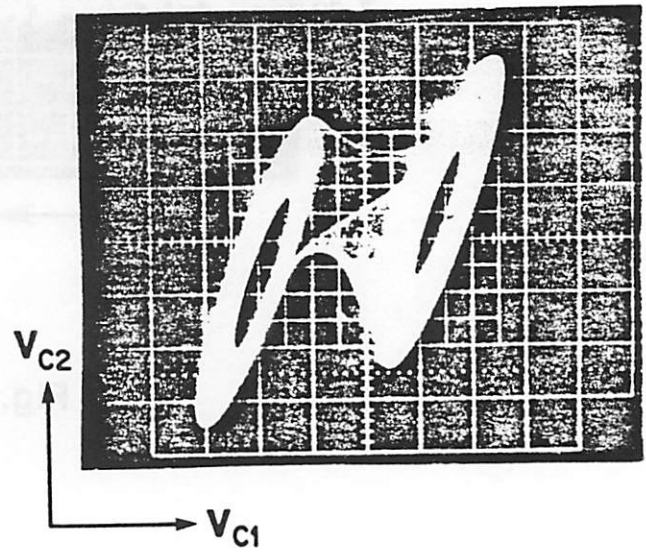
Fig. 16



(a)

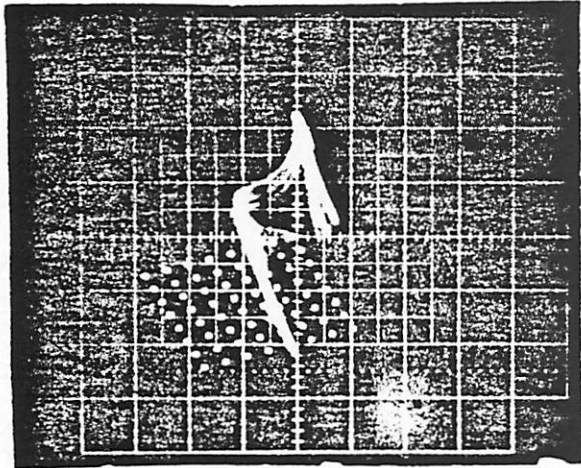


(b)

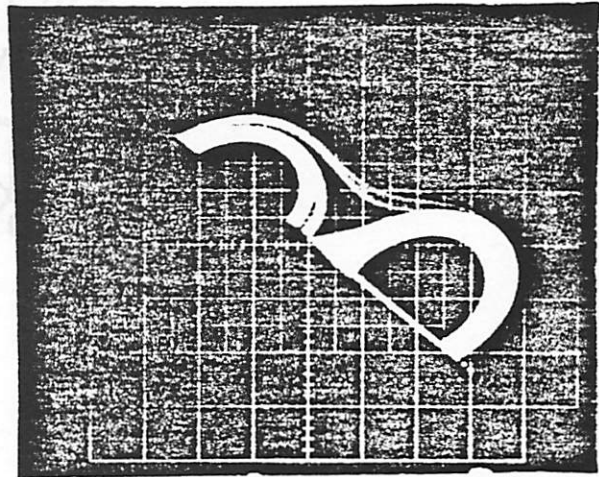


(c)

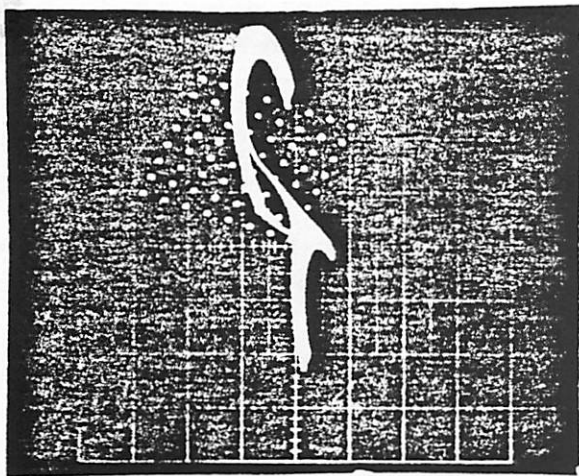
Fig. 17



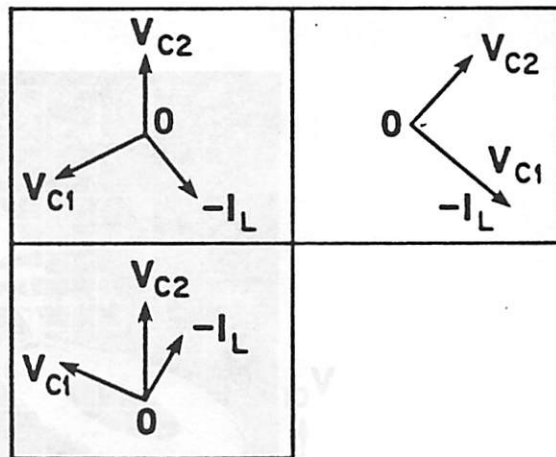
(a)



(c)

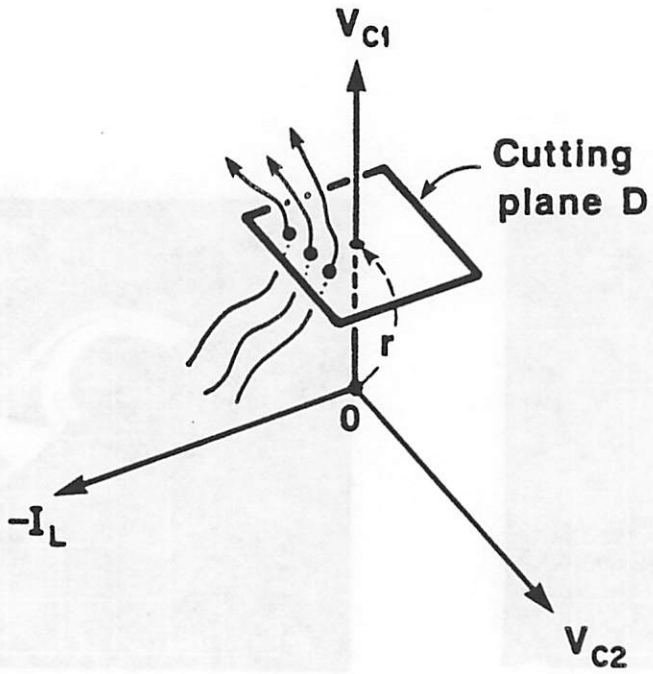


(b)

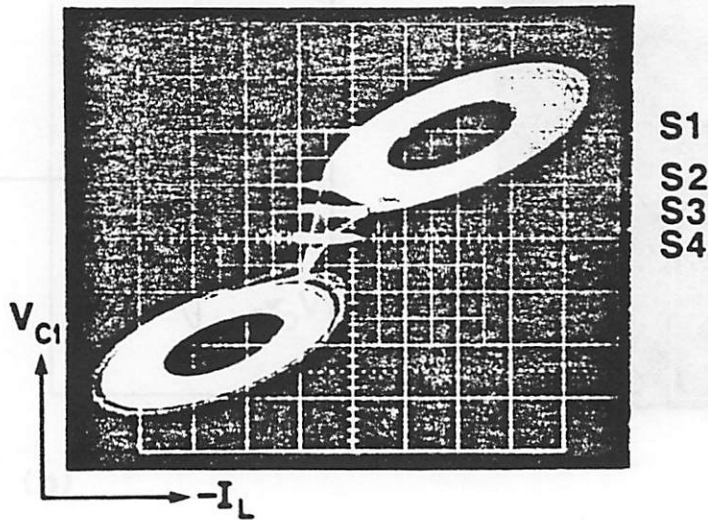


(d)

Fig. 18

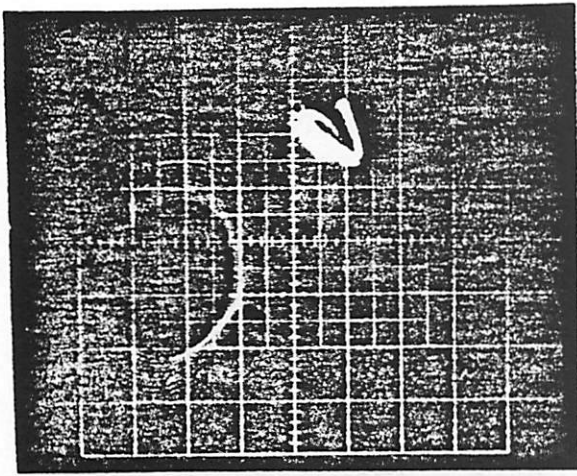


(a)

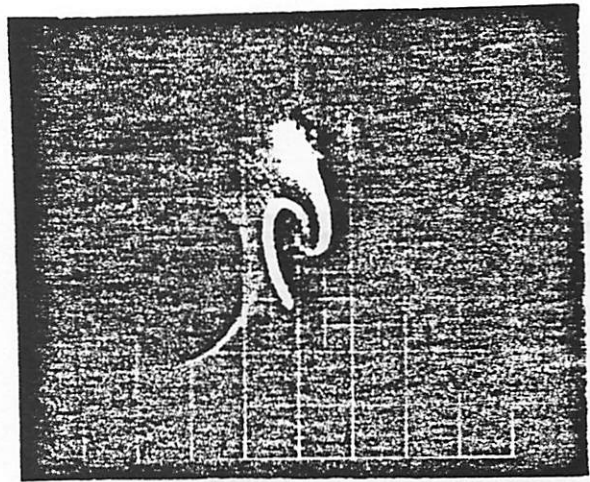


(b)

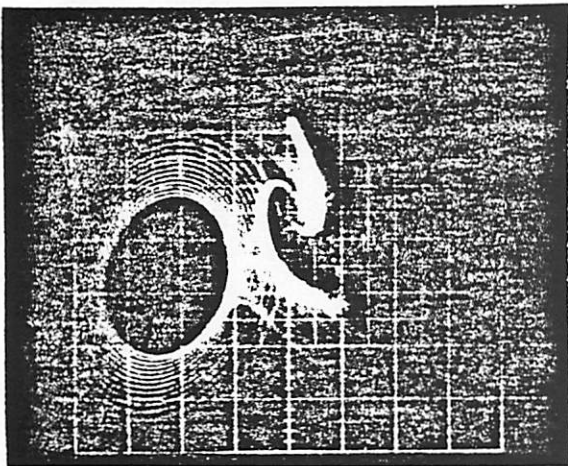
Fig. 19



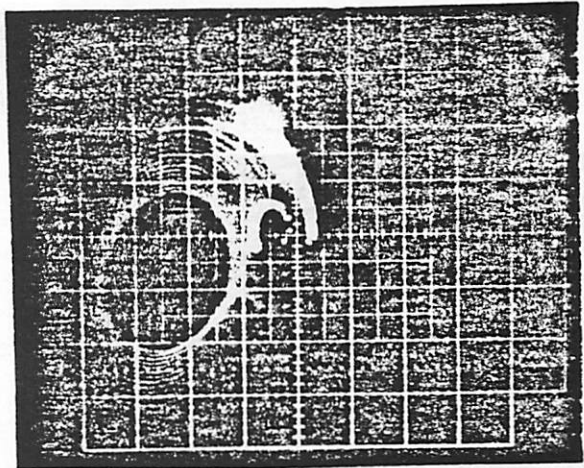
(a)



(c)



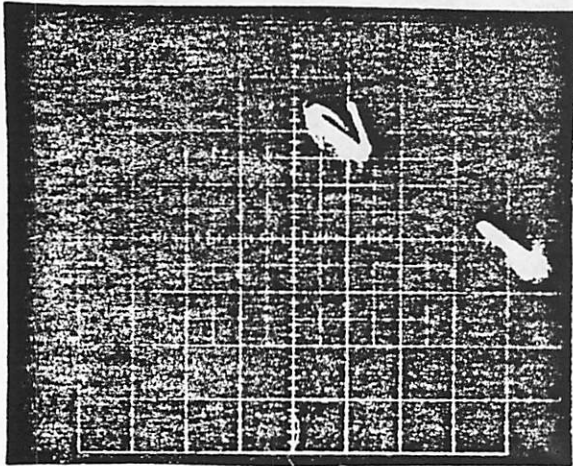
(b)



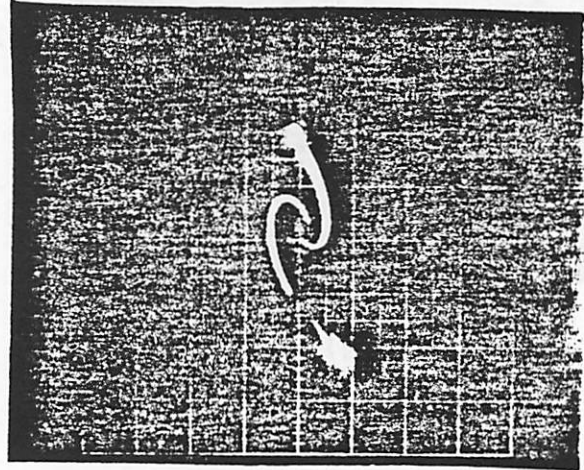
(d)

Fig. 20

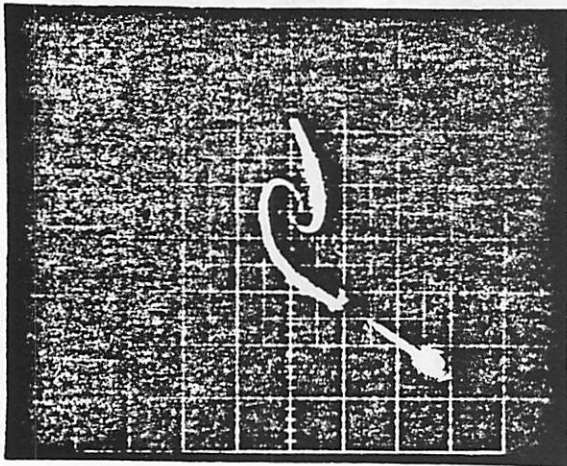
Fig. 20



(a)

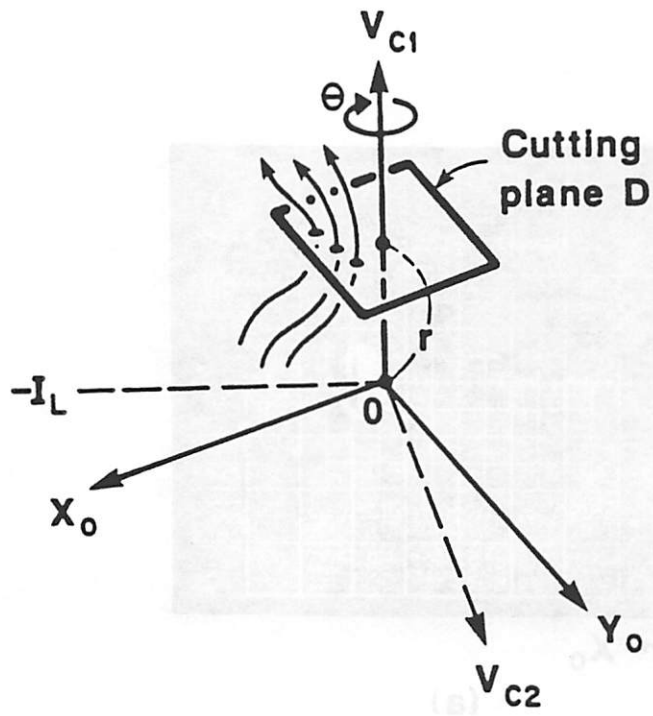


(c)

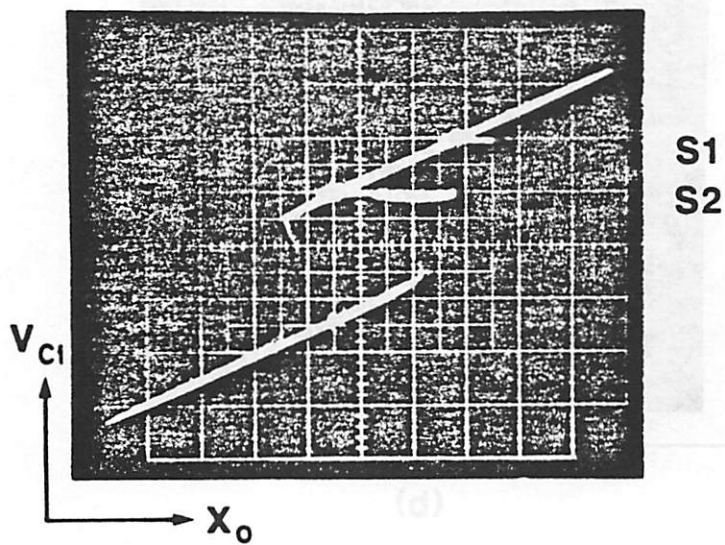


(b)

Fig. 21

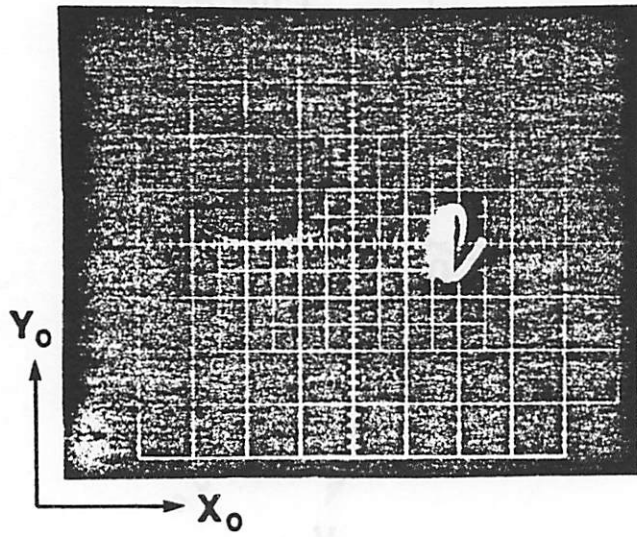


(a)

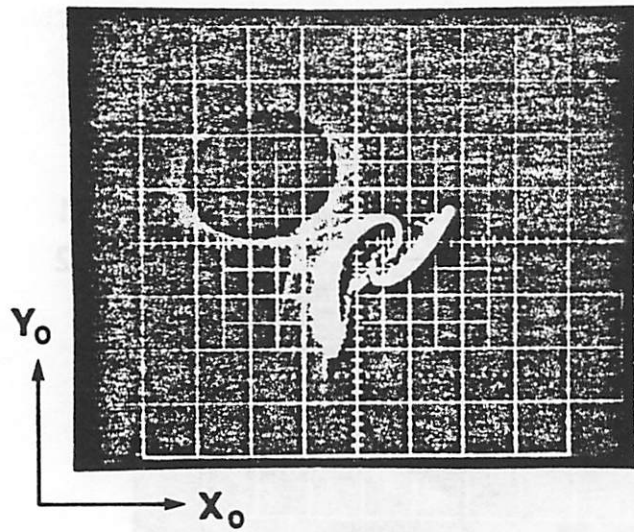


(b)

Fig. 22

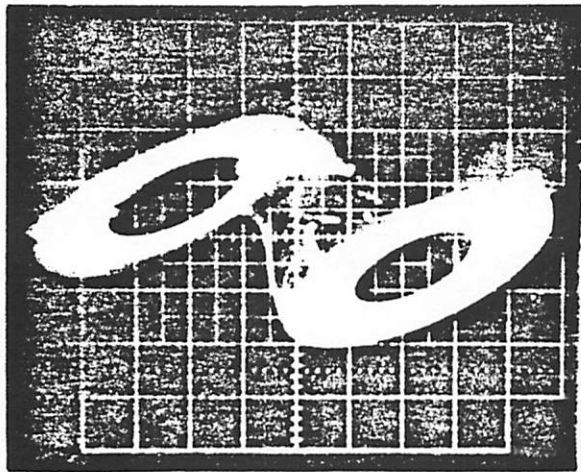


(a)

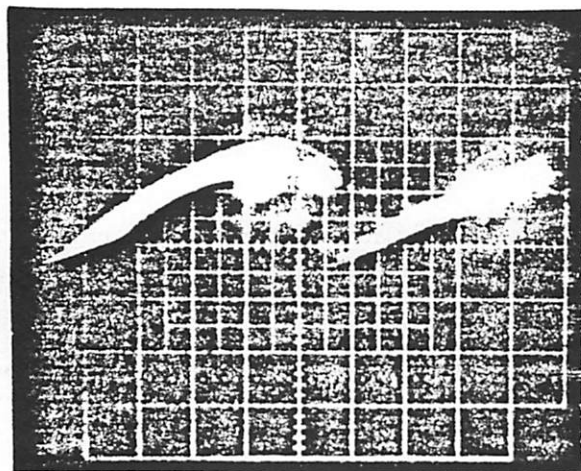


(b)

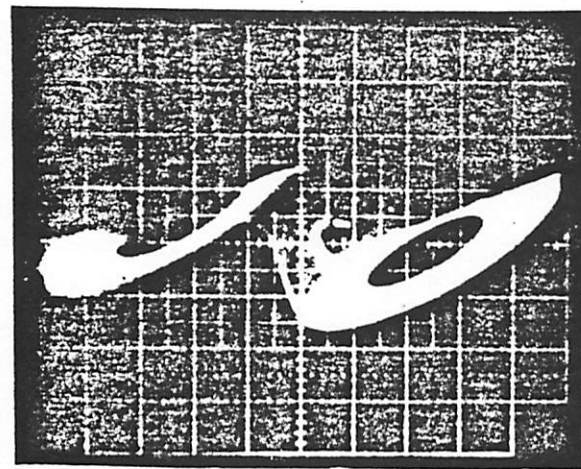
Fig. 23



(a)



(b)



(c)

Fig. 24

APPENDIX

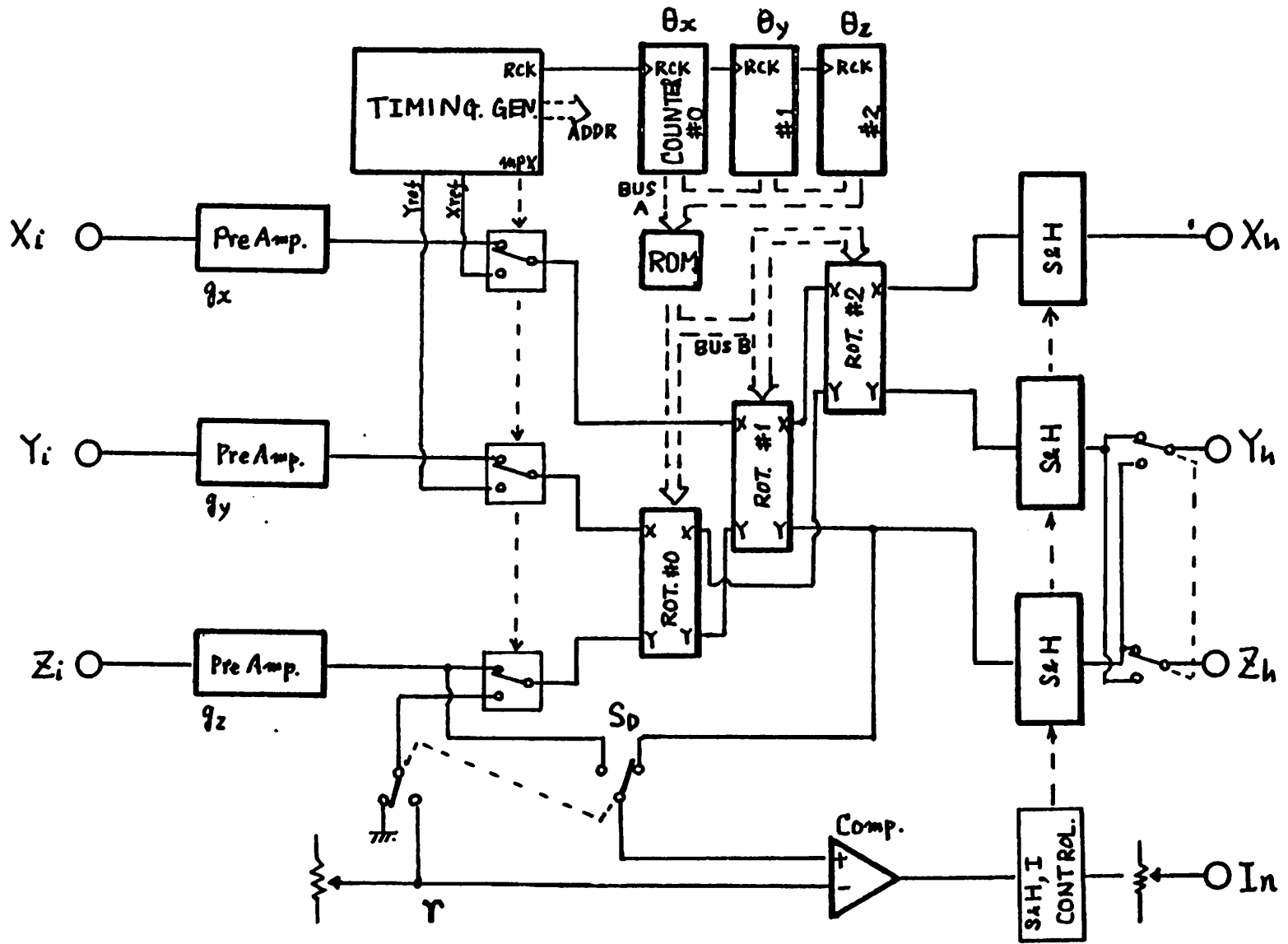


Fig. A-1

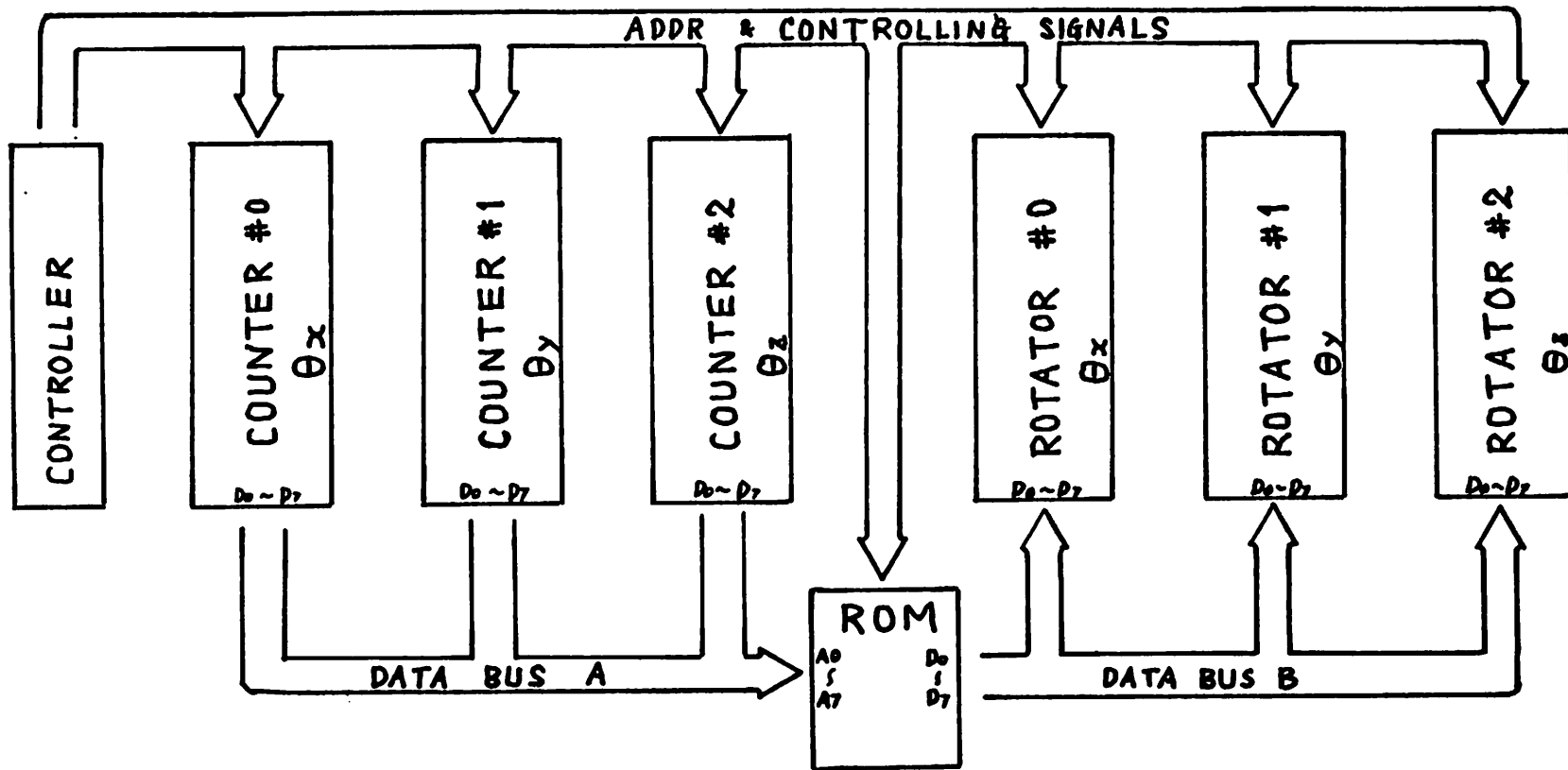


Fig. A-2

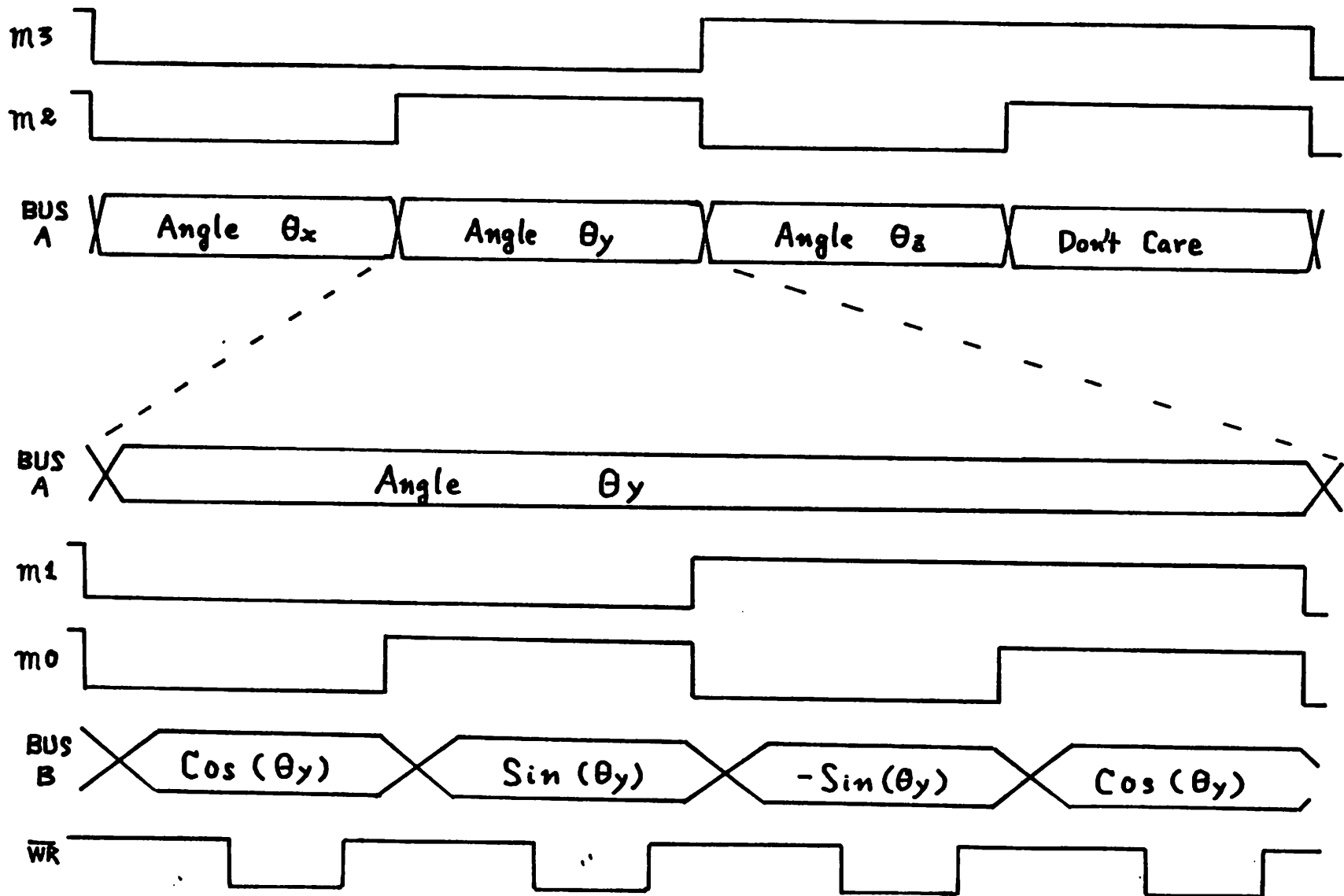


Fig. A-3

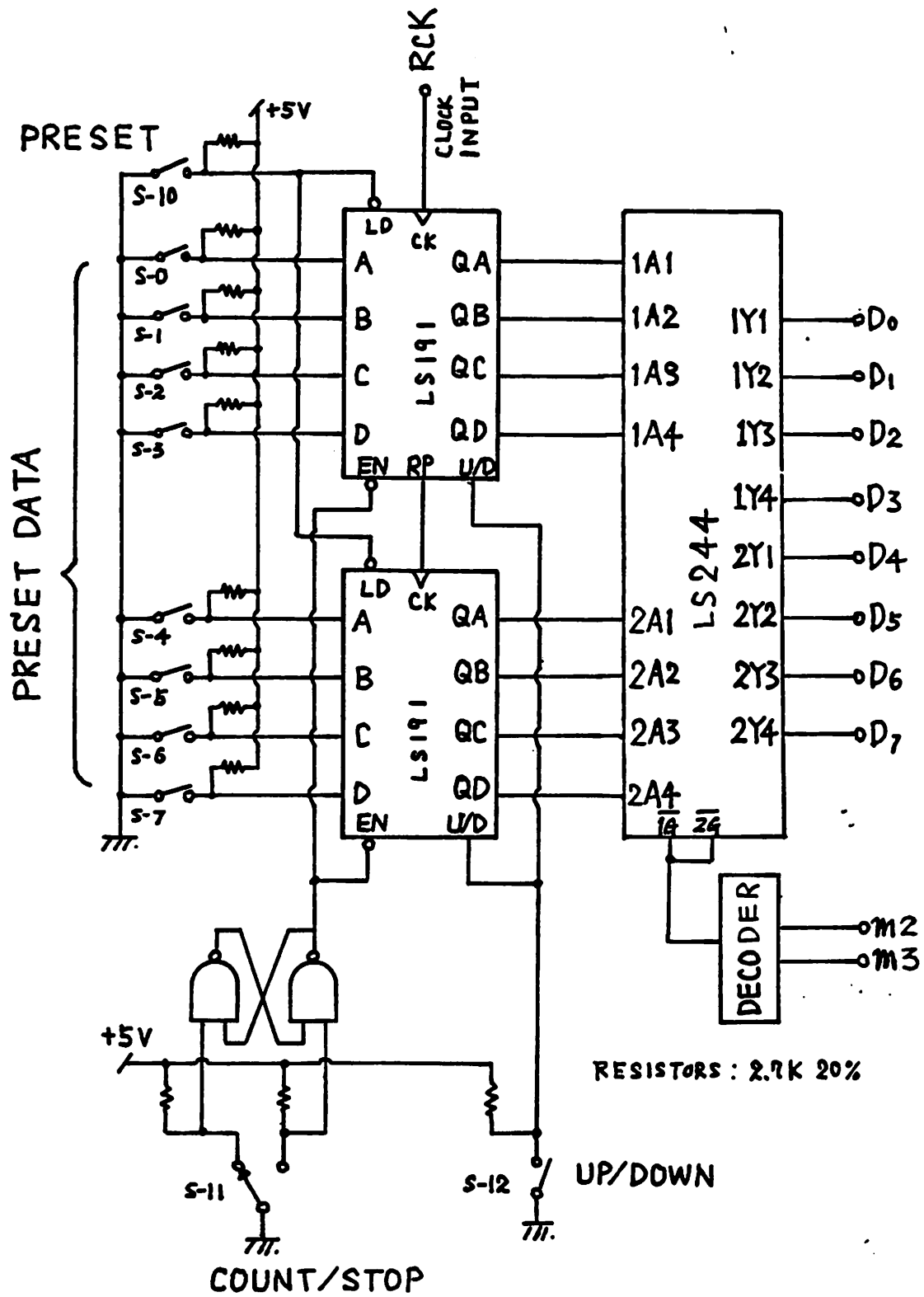


Fig. A-4

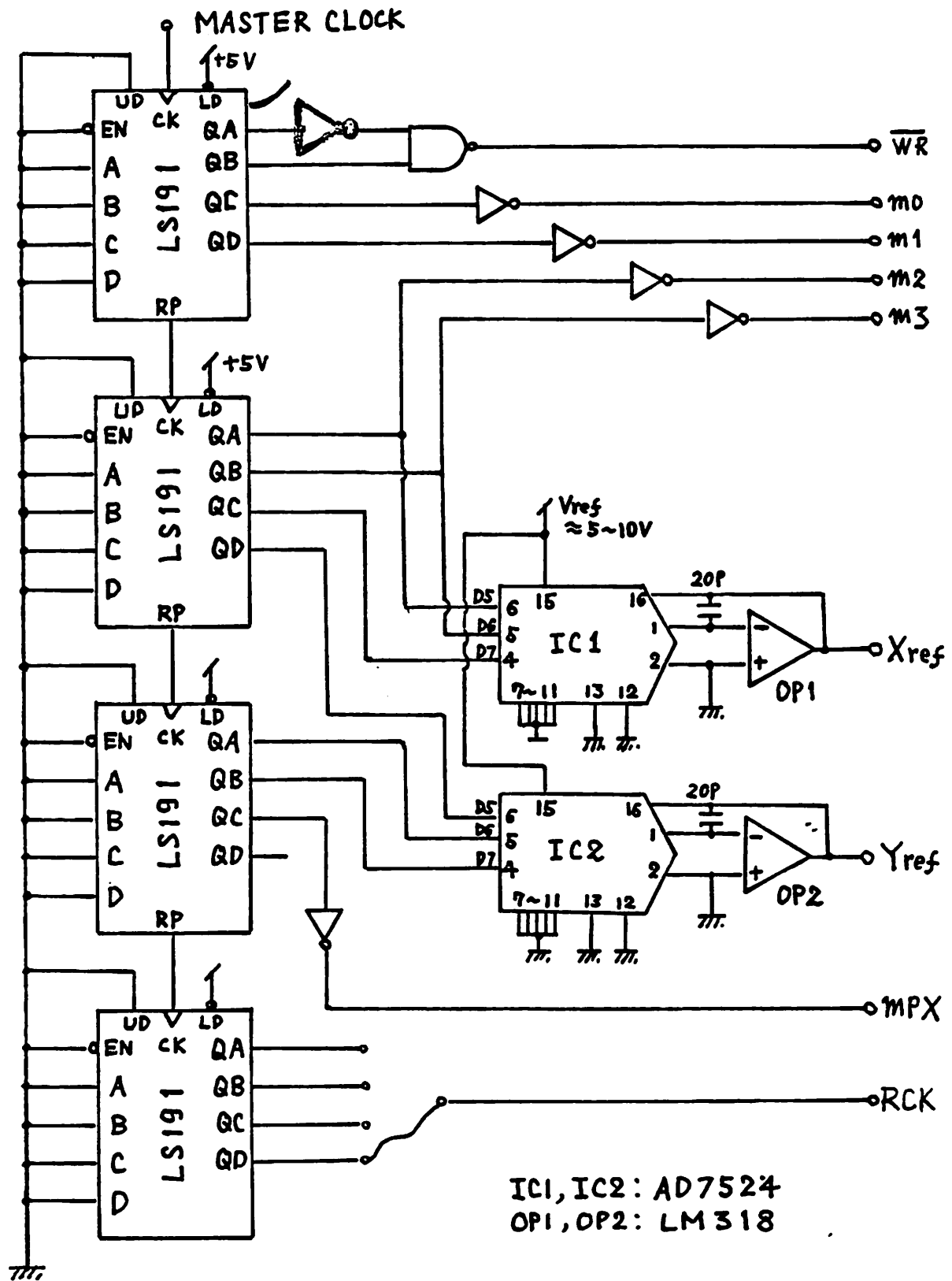


Fig. A-5

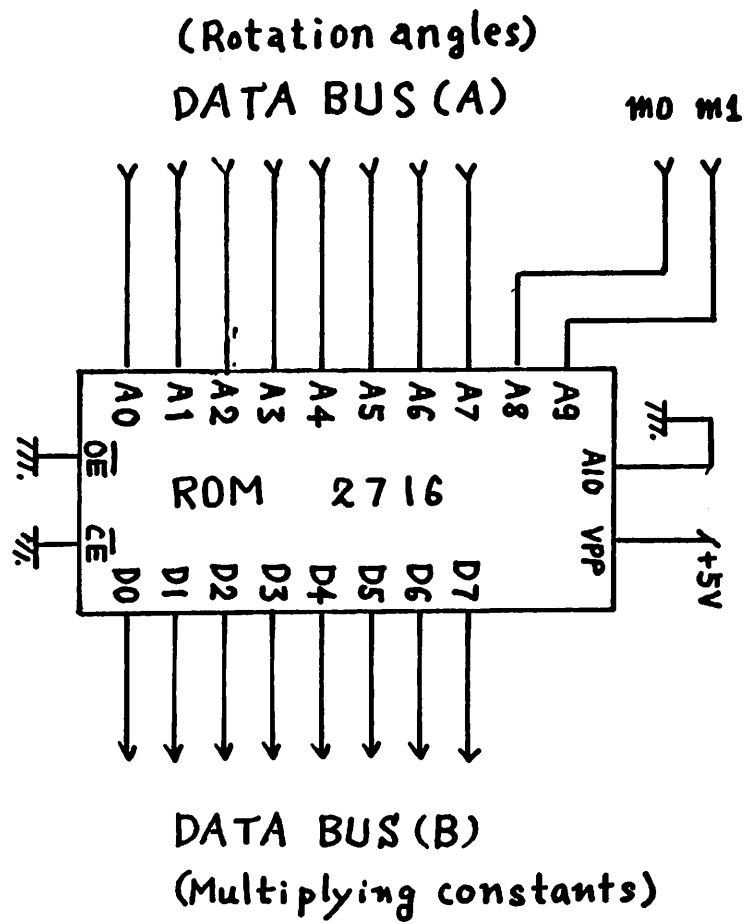


Fig. A-6

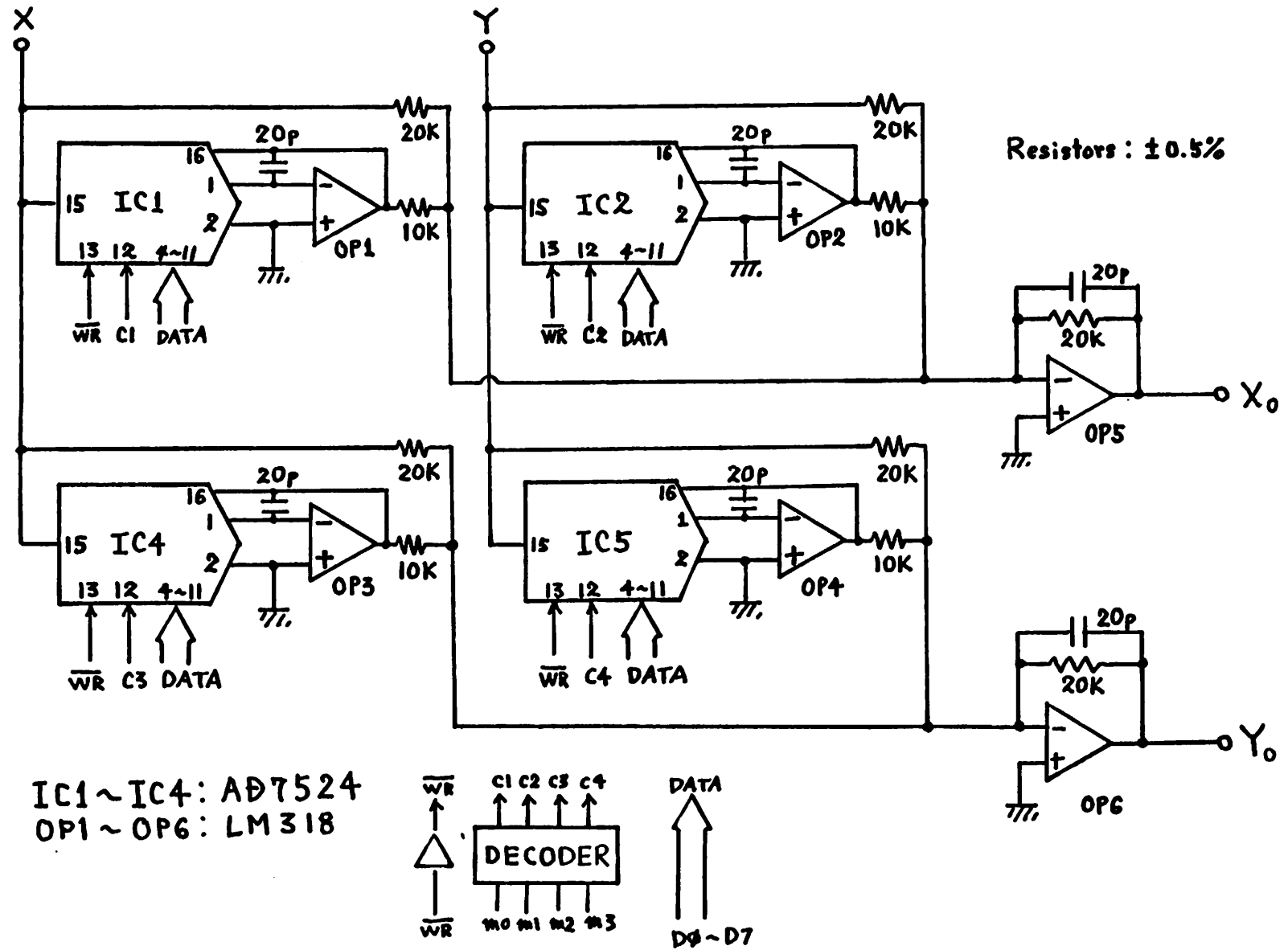


Fig. A-7

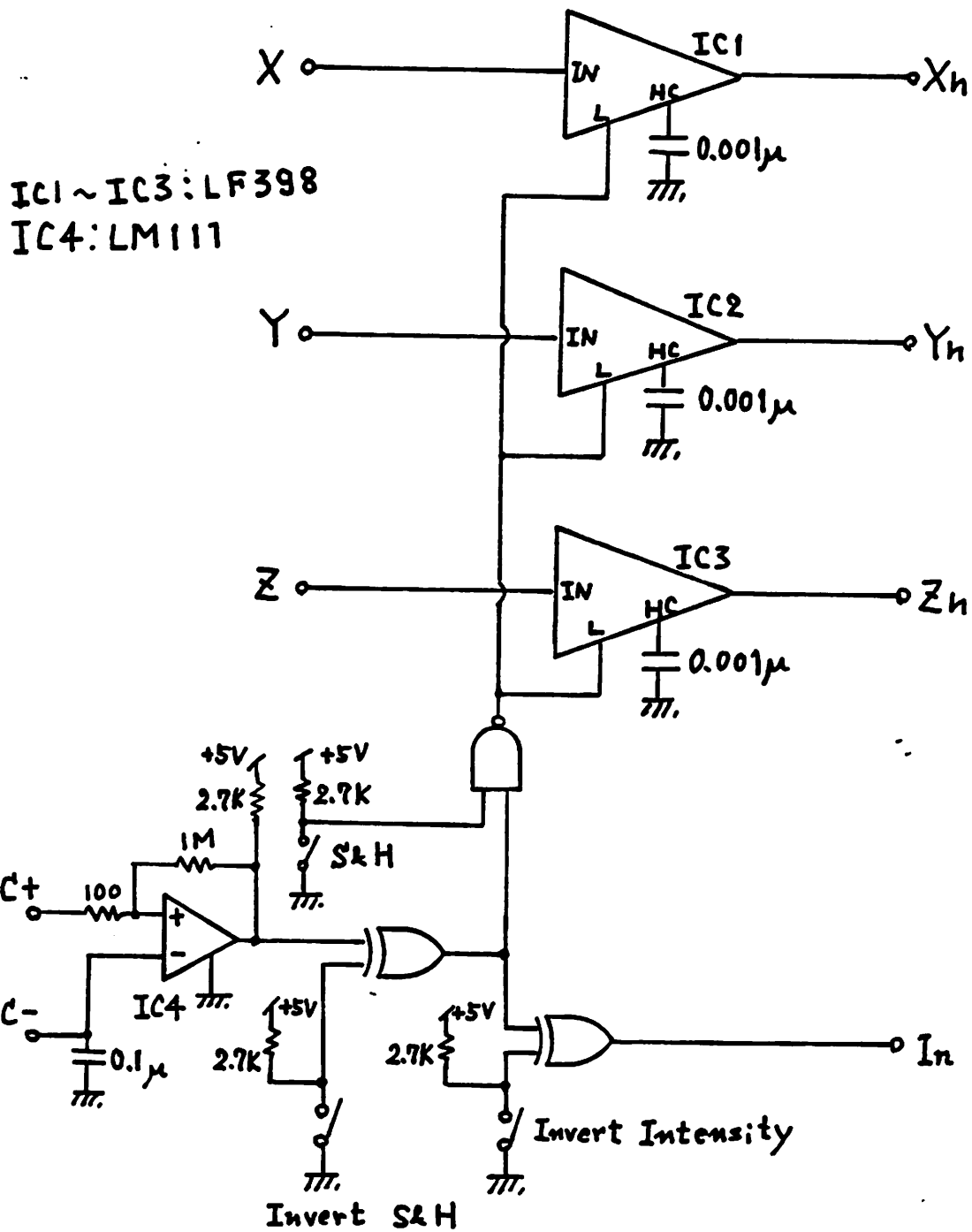


Fig. A-8

000H ~ 0FFH COS(θ) (SAME FOR 300H ~ 3FFH)																
0:	FF	FF	FF	FF	FE	FE	FE	FD	FD	FC	FB	FA	FA	F9	F8	F6
10:	F5	F4	F3	F1	F0	EE	ED	EB	EA	EB	E6	E4	E2	E0	DE	DC
20:	DA	D7	D5	D3	D0	CE	CB	C9	C6	C4	C1	BE	BC	B9	B6	B3
30:	BO	AD	AA	A7	A5	A2	9E	9B	98	95	92	8F	8C	89	86	83
40:	80	7C	79	76	73	70	6D	6A	67	64	61	5D	5A	58	55	52
50:	4F	4C	49	46	43	41	3E	3B	39	36	34	31	2F	2C	2A	28
60:	25	23	21	1F	1D	1B	19	17	15	14	12	11	F	E	C	B
70:	A	9	7	6	5	5	4	3	2	2	1	1	1	0	0	0
80:	0	0	0	0	1	1	1	2	2	3	4	5	5	6	7	9
90:	A	B	C	E	F	11	12	14	15	17	19	1B	1D	1F	21	23
A0:	25	28	2A	2C	2F	31	34	36	39	3B	3E	41	43	46	49	4C
B0:	4F	52	55	58	5A	5D	61	64	67	6A	6D	70	73	76	79	7C
C0:	80	83	86	89	8C	8F	92	95	98	9B	9E	A2	A5	A7	AA	AD
D0:	BO	B3	B6	B9	BC	BE	C1	C4	C6	C9	CB	CE	D0	D3	D5	D7
E0:	DA	DC	DE	E0	E2	E4	E6	E8	EA	EB	ED	EE	F0	F1	F3	F4
F0:	F5	F6	F8	F9	FA	FA	FB	FC	FD	FD	FE	FE	FE	FF	FF	FF
100H ~ 1FFH SIN(θ)																
0:	80	83	86	89	8C	8F	92	95	98	9B	9E	A2	A5	A7	AA	AD
10:	BO	B3	B6	B9	BC	BE	C1	C4	C6	C9	CB	CE	D0	D3	D5	D7
20:	DA	DC	DE	E0	E2	E4	E6	E8	EA	EB	ED	EE	F0	F1	F3	F4
30:	F5	F6	F8	F9	FA	FA	FB	FC	FD	FD	FE	FE	FE	FF	FF	FF
40:	FF	FF	FF	FF	FE	FE	FE	FD	FD	FC	FB	FA	FA	F9	F8	F6
50:	F5	F4	F3	F1	F0	EE	ED	EB	EA	EB	E6	E4	E2	E0	DE	DC
60:	DA	D7	D5	D3	D0	CE	CB	C9	C6	C4	C1	BE	BC	B9	B6	B3
70:	BO	AD	AA	A7	A5	A2	9E	9B	98	95	92	8F	8C	89	86	83
80:	80	7C	79	76	73	70	6D	6A	67	64	61	5D	5A	58	55	52
90:	4F	4C	49	46	43	41	3E	3B	39	36	34	31	2F	2C	2A	28
A0:	25	23	21	1F	1D	1B	19	17	15	14	12	11	F	E	C	B
B0:	A	9	7	6	5	5	4	3	2	2	1	1	1	0	0	0
C0:	0	0	0	0	1	1	1	2	2	3	4	5	5	6	7	9
D0:	A	B	C	E	F	11	12	14	15	17	19	1B	1D	1F	21	23
E0:	25	28	2A	2C	2F	31	34	36	39	3B	3E	41	43	46	49	4C
F0:	4F	52	55	58	5A	5D	61	64	67	6A	6D	70	73	76	79	7C
200H ~ 2FFH -SIN(θ)																
0:	80	7C	79	76	73	70	6D	6A	67	64	61	5D	5A	58	55	52
10:	4F	4C	49	46	43	41	3E	3B	39	36	34	31	2F	2C	2A	28
20:	25	23	21	1F	1D	1B	19	17	15	14	12	11	F	E	C	B
30:	A	9	7	6	5	5	4	3	2	2	1	1	1	0	0	0
40:	0	0	0	0	1	1	1	2	2	3	4	5	5	6	7	9
50:	A	B	C	E	F	11	12	14	15	17	19	1B	1D	1F	21	23
60:	25	28	2A	2C	2F	31	34	36	39	3B	3E	41	43	46	49	4C
70:	4F	52	55	58	5A	5D	61	64	67	6A	6D	70	73	76	79	7C
80:	80	83	86	89	8C	8F	92	95	98	9B	9E	A2	A5	A7	AA	AD
90:	BO	B3	B6	B9	BC	BE	C1	C4	C6	C9	CB	CE	D0	D3	D5	D7
A0:	DA	DC	DE	E0	E2	E4	E6	E8	EA	EB	ED	EE	F0	F1	F3	F4
B0:	F5	F6	F8	F9	FA	FA	FB	FC	FD	FD	FE	FE	FE	FF	FF	FF
C0:	FF	FF	FF	FF	FE	FE	FE	FD	FD	FC	FB	FA	FA	F9	F8	F6
D0:	F5	F4	F3	F1	F0	EE	ED	EB	EA	E8	E6	E4	E2	E0	DE	DC
E0:	DA	D7	D5	D3	D0	CE	CB	C9	C6	C4	C1	BE	BC	B9	B6	B3
F0:	BO	AD	AA	A7	A5	A2	9E	9B	98	95	92	8F	8C	89	86	83

Table A-1